The Transparent Nucleus: unperturbed inverse kinematics nucleon knockout measurements with a 48 GeV/c carbon beam

(The BM@N Collaboration)

From superconductors to atomic nuclei, dense strongly-interacting many-body systems are ubiquitous in nature. Measuring the ground-state distribution of particles in such systems is a formidable challenge, often met by particle knockout scattering experiments [1–9]. However, quantum mechanics imposes a fundamental limitation on interpreting such measurements due to interferences of initial- and final-state interactions (ISI/FSI) between the incoming and scattered particles and the residual system [1, 10–13]. This is a fundamental limitation for probing the microscopic structure of atomic nuclei. Here we overcome this by measuring the quasi-free scattering of 48 GeV/c ^{12}C ions from hydrogen. The distribution of single nucleons is studied by detecting two protons at large angles in coincidence with an intact ^{11}B nucleus. The ^{11}B detection is shown to select the transparent part of the reaction and exclude the otherwise large ISI/FSI contributions that would break the ^{11}B apart. By detecting residual ^{10}B and ^{10}Be nuclei, we further identified short-range correlated (SRC) nucleon-nucleon pairs [13–15], and establish the separation of the pair wave-function from that of the residual nuclear system [13, 16]. All measured reactions are well described by theoretical calculations that do not contain ISI/FSI. Our results thus showcase a new ability to study the short-distance structure of short-lived radioactive atomic nuclei at the forthcoming FAIR [17] and FRIB [18] facilities. These studies will be pivotal for developing a ground-breaking microscopic understanding of nuclei far from stability and of cold dense nuclear systems such as neutron stars.

Strongly-interacting systems are difficult to study. In the special case of strongly-interacting atoms in ultra-cold traps, ground-state properties can be directly measured by instantaneously turning off the interactions between the atoms and the trap itself [19]. This allows exploring a wide range of fundamental quantum mechanical phenomena and to imitate strongly correlated states in condensed matter systems where similar control over inter-particle interactions cannot be obtained [20].

Due to their high-density and complex strong interaction, constructing such model systems for atomic nuclei is extremely challenging. Instead, the distribution of nucleons in nuclei is traditionally studied using high-energy electron scattering experiments that detect the scattered electron and knockout nucleon with high-resolution spectrometers. Pre-selection of the reaction kinematics or post-selection of the un-detected residual nucleus allows suppressing ISI/FSI effects and use energy and momentum conservation to reconstruct the distribution of nucleons in the nucleus [1, 13, 14, 21–23].

While largely limited to stable nuclei, such experiments helped establish the nuclear shell model [1, 2] and the existence of SRC nucleon pairs [13, 14] that constitute the next significant approximation to nuclear structure after the shell model.

Extending these studies to radioactive nuclei far from nuclear stability is a growing frontier of nuclear science. Such studies require performing scattering experiments in inverse kinematics, where low luminosity high-energy beams of radioactive nuclei are scattered from protons in hydrogen targets [24]. The cross-section for such reactions is significantly higher than that for electron scattering, but comes at the price of large ISI that prevents kinematical pre-selection. Additionally, since there is rarely sufficient energy resolution to determine the residual nuclear state from the measured momenta of the knocked-out nucleons, post-selection requires direct detection of the residual nuclear system.

Here we use post-selection in high-energy inverse kinematics $(p, 2p)$ scattering to probe single-particle states and SRCs in the well understood ^{12}C nucleus. By detecting a bound nuclear fragment we select the transparent part of the scattering reaction where neither the incoming proton nor the outgoing nucleons undergo ISI/FSI.

By identifying ^{11}B fragment we successfully study the distribution of protons in the p-shell of ^{12}C, where we obtain consistent distributions for both quasielastic (QE) and inelastic (IE) scattering reactions. Selecting ^{10}B and ^{10}Be fragments we further identify, for the first time in inverse kinematics, the hard breakup of SRC pairs. We directly measure the pair motion in the nucleus and establish the separation of the strong inter-pair interaction from the residual nuclear system.

While significantly reducing the measured event rate, these post-selection requirements are shown to ensure that the measured reaction has little to no sensitivity to ISI/FSI, thereby opening the door to studying the single-particle and short-distance structure of nuclei far from stability.

Experimental setup

The experiment took place at the Joint Institute for Nuclear Research (JINR), using a 4 GeV/c/nucleon ion beam from the Nuclotron accelerator, a stationary liquid-hydrogen target, and a modified BM@N (Baryonic Mat-

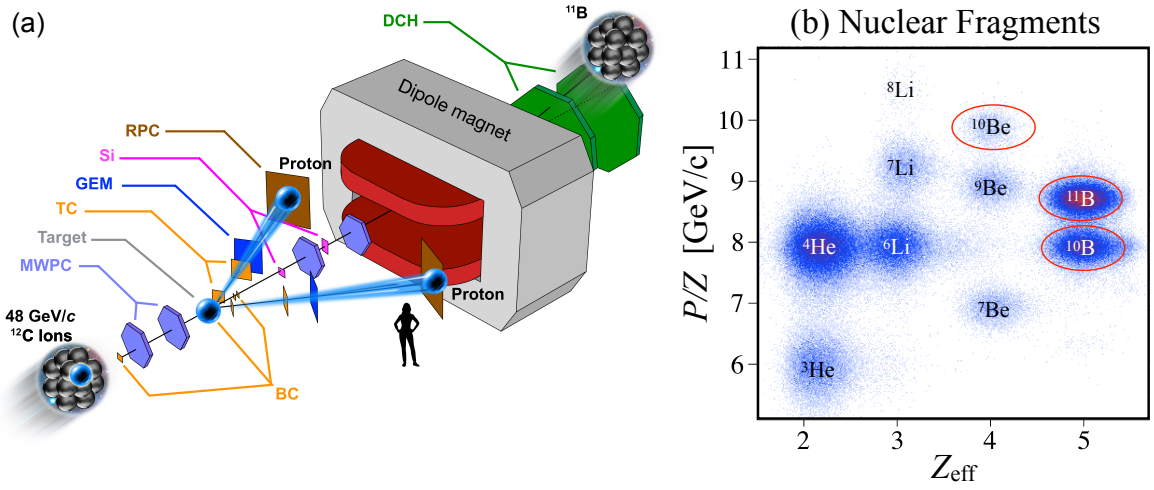

Fig. 1. | **Experimental Setup and Fragment Identification.** (a) Carbon nuclei traveling at 48 GeV/c hit protons in a liquid hydrogen target, knocking out individual protons from the beam-ion. Position- and time-sensitive detectors (MWPC, GEM, RPC, Si, and DCH) are used to track the incoming ion beam, knockout protons, and residual nuclear fragments and determine their momenta. (b) The bend of the nuclear fragments in the large dipole magnet, combined with charge measurements with the beam counters (BC) allows identifying the various fragments. In this work we refer to events with detected ^{11}B, ^{10}B, and ^{10}Be heavy fragments, see text for details.

ter at Nuclotron) experimental setup, as shown in Fig. 1a.

The beam was monitored upstream the target using thin scintillator-based beam counters (BCs) used for charge identification, a beam-halo veto beam counter (V-BC), and two multi-wire proportional chambers (MWPCs) for event-by-event beam tracking. The BC closer to the target was also used to define the event start time t_0.

A two-arm spectrometer (TAS) was placed downstream of the target to detect the two protons from the $(p, 2p)$ reaction that emerge at $24° - 37°$, corresponding to 90° QE scattering in the two-protons center-of-mass (c.m) frame. Each spectrometer arm consisted of two scintillator trigger counters (TC), a gas electron multiplier (GEM) station and a multi-gap resistive plate chamber (RPC) wall.

Proton tracks were reconstructed using their hit location in the GEM and RPC walls. We only consider events where the interaction vertex of each proton is reconstructed within the central 26 cm of the target and the distance between them is smaller than 4 cm (Extended Data Fig. 1). The time difference between the RPC and t_0 signals define the proton time of flight (TOF), that is used to determine its momentum from the measured track length, assuming a proton mass.

As the protons of interest for our analysis have momenta between 1.5 and 2.5 GeV/c ($\beta = 0.85 = 0.935$), we conservatively reject events with proton tracks having $\beta > 0.96$ or < 0.8.

Signals from the TC were combined with the BCs upstream the target to form the main ^{12}C$(p, 2p)$ reaction trigger for the experiment. Additional triggers were set up for monitoring and calibration purposes, see online supplementary materials for details.

Nuclear fragments following the $(p, 2p)$ reaction are emitted at small angles with respect to the incident beam with momentum that is similar to the beam momentum. Three silicon (Si) planes and two MWPCs were placed in the beam-line downstream the target to measure the fragment scattering angle. Following the MWPCs the fragments enter a large acceptance 2.87 T·m dipole magnet. Two drift chambers (DCH) are used to measure the fragment trajectory after the magnet.

The fragment momenta are determined from their measured bending angle in the magnet. Fragments are identified from the combination of their bend angle in the magnet and energy deposition in the two scintillator BCs placed between the target and the magnet entrance, see Fig. 1b. The latter is proportional to the sum of all fragment charges squared ($Z_{\rm eff} = \sqrt{\sum Z^2}$).

See Methods and online supplementary materials for additional details on the experimental setup and data analysis procedures.

Single proton knockout

We identify exclusive ^{12}C$(p, 2p)^{11}$B events by requiring the detection of a ^{11}B fragment in coincidence with two charged particle tracks in the TAS. Energy and momentum conservation for this reaction reads:

$$\bar{p}_{^{12}\rm C} + \bar{p}_{tg} = \bar{p}_1 + \bar{p}_2 + \bar{p}_{^{11}\rm B}, \qquad (1)$$

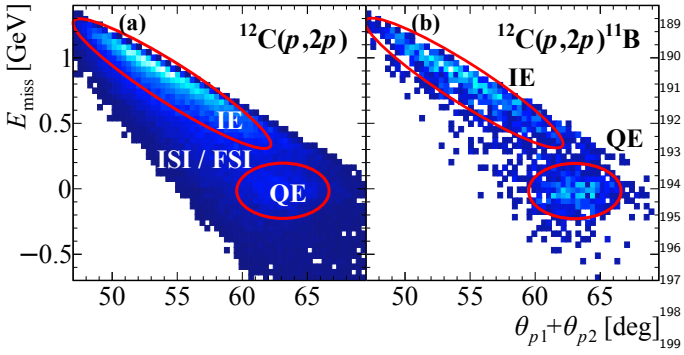

Fig. 2. | Quasi-Free Scattering (QFS) Distributions. The correlation between the measured missing-energy $E_{\rm miss}$, calculated in the ^{12}C rest-frame, and the measured lab-frame two-proton in-plane opening angle. Distributions are shown for (a) ^{12}C$(p,2p)$ and (b) ^{12}C$(p,2p)^{11}$B events. Quasielastic (QE) events are seen as a peak around low missing energy and opening angles of $\sim 63^\circ$ that is marked by a red oval. Inelastic (IE) reactions populate higher missing-energy and lower opening angles while ISI/FSI populate both regions and the ridge between them in the inclusive spectra.

where $\bar{p}_{^{12}\rm C} = (\sqrt{(\mathbf{p}^2_{^{12}\rm C} + m^2_{^{12}\rm C}}), 0, 0, p_{^{12}\rm C})$ and $\bar{p}_{tg} = (m_p, 0, 0, 0)$ are respectively the incident beam-ion and target proton four-momentum vectors. $\bar{p}_1$, $\bar{p}_2$, and $\bar{p}_{^{11}\rm B}$ are the four-momentum vectors of the detected protons and ^{11}B fragment. Assuming QE scattering off a mean-field nucleon we can approximate $\bar{p}_{^{12}\rm C} = \bar{p}_i + \bar{p}_{^{11}\rm B}$, where $\bar{p}_i$ is the initial proton four-momentum inside the ^{12}C ion. Substituting into Eq. 1 we obtain:

$$\bar{p}_i \approx \bar{p}_{\rm miss} \equiv \bar{p}_1 + \bar{p}_2 - \bar{p}_{tg}, \qquad (2)$$

where $\bar{p}_{\rm miss}$ is the measured missing four-momentum of the reaction and is only equal to $\bar{p}_i$ in the case of unperturbed (no ISI/FSI) QE scattering. Through the text, the missing momentum vector is shown and discussed after being boosted from the lab-frame to the ^{12}C ion rest-frame.

Figure 2 shows the measured missing energy $E_{\rm miss} \equiv m_p - e_{\rm miss}$ (where $e_{\rm miss}$ is the energy component of $\bar{p}_{\rm miss}$ in the ^{12}C rest-frame) vs. the lab-frame two-proton in-plane opening angle, $\theta_1 + \theta_2$. Distributions are shown for ^{12}C$(p,2p)$ (left panel) and ^{12}C$(p,2p)^{11}$B (right panel) events. Both distributions show two distinct regions: (A) low missing-energy and large in-plane opening angles that correspond to QE scattering and (B) high missing-energy and small in-plane opening angles that correspond to inelastic (IE) scattering.

The inclusive ^{12}C$(p,2p)$ events are contaminated by ISI/FSI backgrounds around and underlying both IE and QE regions (see Extended Data Fig. 2 for 1D projections). This background is not evident in the ^{12}C$(p,2p)^{11}$B case, which is our first indication that requiring the coincidence detection of ^{11}B fragments selects a unique subset of one-step processes where a single nucleon was knocked-out without any further interaction with the residual fragment. We note that while bound excited states cannot be separated from the ground state in ^{12}C$(p,2p)^{11}$B events, their contribution is small [25] and should not impact the measured momentum distribution. See Methods for details.

Fig. 3a shows further evidence for ISI/FSI suppression by comparing the measured missing-momentum distribution for ^{12}C$(p,2p)$ QE events with and without ^{11}B tagging. The QE selection was done using the missing-energy and in-plane opening-angle cuts depicted in Fig. 2 following a 2σ selection (see Methods for details). The measured ^{12}C$(p,2p)$ QE events show a significant high-momentum tail that extends well beyond the nuclear Fermi-momentum ($\approx$ 250 MeV/c) and is characteristic for ISI/FSI [13]. This tail is completely suppressed by the ^{11}B detection.

Figure 3b compares the measured ^{11}B momentum distribution in the ^{12}C rest-frame for both QE and IE ^{12}C$(p,2p)^{11}$B events. The fragment momentum distribution is equal for both reactions. This shows that the observation of a bound fragment selects quasi-free unperturbed single-step reactions, even in the case of inelastic NN scattering and in a kinematical region which is otherwise dominated by FSI events.

In true unperturbed single-step ^{12}C$(p,2p)^{11}$B QE scattering the measured missing- and fragment-momenta should balance each other. Fig. 3c shows the distribution of the cosine of the opening angle between the missing- and fragment-momenta in the plane transverse to the incident beam-ion (which is insensitive to boost effects and is measured with better resolution). While broadened due to our detector resolutions, a clear back-to-back correlation is observed which is a distinct signature of QE reactions.

The data shown in Fig. 3 are compared to theoretical calculations of QE $(p,2p)$ scattering off a p-shell nucleon in ^{12}C. The calculation is implemented via a simulation that accounts for the experimental acceptance and detector resolutions, uses measured ^{1}H$(p,2p)$ elastic scattering cross section, and does not include ISI/FSI effects. The total simulated event yield was scaled to match the data. See methods for details. The calculation well reproduce the measured distribution.

The calculation agrees well with all measured ^{12}C$(p,2p)^{11}$B distributions, including the fragment momentum distribution for IE events. This is a clear indication that the ^{11}B detection strongly suppresses ISI/FSI, providing access to ground-state properties of ^{12}C. Additional data-theory comparisons are shown in Extended Data Fig. 2 and 3.

Our data shows that the ^{12}C$(p,2p)^{11}$B QE events yield account for $(40.3 \pm 2.0\,(\rm stat) \pm 5.5\,(\rm sys))\%$ of the total number of ^{12}C$(p,2p)$ QE events measured in our kinematics. We further measured ^{12}C$(p,2p)^{10}$B and ^{12}C$(p,2p)^{10}$Be events that correspond to QE scattering

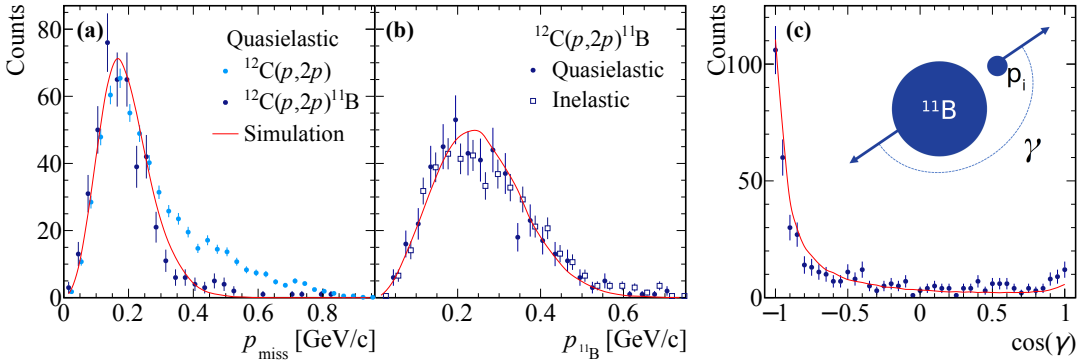

Fig. 3. | **Momentum Distributions.** (a) Missing-momentum distribution in ^{12}C rest-frame for quasielastic ^{12}C$(p,2p)$ and ^{12}C$(p,2p)^{11}$B events. (b) ^{11}B fragment momentum distribution in ^{12}C rest-frame for quasielastic and inelastic ^{12}C$(p,2p)^{11}$B events. The light blue points in (a) and the open symbols in (b) have a small artificial offset for better visibility. (c) Distribution of the cosine of the opening-angle between the missing- and fragment-momentum in the plane transverse to the beam. Solid red line shows the result of our quasielastic reaction simulation. Data error bars show statistical uncertainties at the 1σ confidence level. The y-axis shows the counts for the quasielastic distribution. The inelastic distributions are normalized to the peak region of the quasielastic distribution. All variables are shown in the ^{12}C rest-frame.

to an excited ^{11}B state that de-excites via neutron or proton emission respectively. These events correspond to $(11.1 \pm 1.1\,(\text{stat}) \pm 1.5\,(\text{sys}))\%$ (^{10}B) and $\leq 2\%$ (^{10}Be) of the total number of ^{12}C$(p,2p)$ QE events. See Methods section for details. Therefore, in $\sim 50\%$ of the measured ^{12}C$(p,2p)$ QE events the residual nucleus is fragmented to lighter fragments ($Z < 4$).

Hard Breakup of SRC Pairs

Next we study SRCs by selecting ^{12}C$(p,2p)^{10}$B and ^{12}C$(p,2p)^{10}$Be events. SRC breakup reactions produce ^{10}B and ^{10}Be fragments when interacting with a proton-neutron (pn) or proton-proton (pp) pair, respectively. The fragment selection guarantees exclusion of secondary scattering processes as shown in the previous section. It implies also a selection of an excitation-energy window of the residual A-2 system corresponding to its nucleon separation energy. As pn-SRC were shown to be 20 times more abundant than pp-SRC pairs [26–30], we expect to observe 10 times more ^{10}B fragments than ^{10}Be. The latter have 2 times larger contribution to the cross-section as the reaction can take place off either proton in the pair.

^{10}B and ^{10}Be fragments can also be formed due to QE single-proton knockout, as discussed above, that results in an excited ^{11}B fragment that de-excites via nucleon emission. In this case the $(p,2p)$ part of the reaction should be identical to the QE ^{11}B process, except the ^{10}B or ^{10}Be momenta will not strongly correlate with $\mathbf{p}_{\text{miss}}$.

An interaction with a nucleon that is part of an SRC pair will be significantly different. The high relative momentum of nucleons in SRC pairs leads to a large value of $\mathbf{p}_i$ that is largely balanced by a single correlated nucleon, as oppose to the entire $A-1$ nucleons system. Therefore, we require $|\mathbf{p}_{\text{miss}}| > 350$ MeV/c to select SRC breakup events that are far enough from the Fermi level where contributions from meanfield nucleons are negligible.

IE events where the high-$\mathbf{p}_{\text{miss}}$ is caused by the production of additional particles or by QE interaction followed by FSI that knock out a neutron from the ^{11}B fragment will not be suppressed by this requirement. IE interactions can be suppressed by requiring a large in-plane opening angle between the protons measured in the $(p,2p)$ reaction and restricting the missing-energy of the reaction (Fig. 2).

To guide these selections we used the Generalized Contact Formalism (GCF) [16] to simulate $(p,2p)$ scattering off high missing-momentum SRC pairs. The GCF predicts an in-plane opening angle larger than 63° and $-110 \leq E_{\text{miss}} \leq 240$ MeV (see Methods and Extended Data Fig. 4 for details).

We further apply to the two-proton selection the same vertex and β cuts mentioned above and use total-energy and momentum conservation to ensure exclusivity by requiring a missing nucleon mass in the entire reaction: $M^2_{\text{miss, excl.}} = (\bar{p}_{^{12}\text{C}} + \bar{p}_{tg} - \bar{p}_1 - \bar{p}_2 - \bar{p}_{^{10}\text{B(Be)}})^2 \approx m_N^2$ (see Extended Data Fig. 5).

We measured 26 ^{12}C$(p,2p)^{10}$B and 3 ^{12}C$(p,2p)^{10}$Be events that pass the missing-momentum, missing-energy, in-plane opening angle, and total missing mass cuts described above. We note that our measured events rate and ^{10}B to ^{10}Be ratio is inconsistent with being dominated by mean field QE scattering followed by FSI with a single nucleon in ^{11}B and/or de-excitation via nucleon emission. See Methods for details.

Figure 4 shows the missing-energy and missing-momentum distributions of the selected SRC ^{12}C$(p,2p)^{10}$B events. The measured distributions show good agreement with the GCF predictions. Addi-

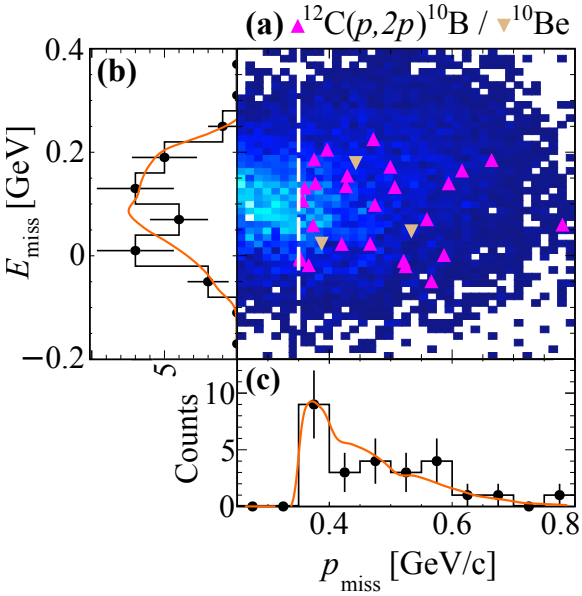

Fig. 4. | SRC Selection in missing momentum and energy. (a) Correlation between the missing-energy and missing-momentum for the measured ^{12}C$(p,2p)^{10}$B (upwards facing purple triangles) and ^{12}C$(p,2p)^{10}$Be (Downwards facing brown triangles) selected SRC events, on top of the GCF simulation (color scale). (b) and (c) one dimensional projections for the measured (black points) and GCF simulated (orange line) missing-energy (b) and missing-momentum (c). Data error bars show statistical uncertainties at the 1σ confidence level.

tional kinematical distributions are shown and compared with the GCF in Extended Data Fig. 6 and 7. We specifically note that the distributions of the z-component of the missing-momentum is not centered around zero and is shifted towards the incident beam-direction. This is expected given the strong s-dependence of the large-angle elementary proton-proton elastic scattering cross-section. See discussion in Methods.

Next we examine the angular correlations between the nucleons in the pair and between the pair and the ^{10}B fragment. Figure 5a shows the distribution of the cosine of the angle between the missing momentum (Eq. 2) and the undetected recoil nucleon momentum. The latter is reconstructed using total energy and momentum conservation. A clear back-to-back correlation is observed, as expected for strongly-correlated nucleon pairs. The width of the distribution is driven by the pair c.m. motion. It shows good agreement with the GCF prediction that assumes a three-dimensional Gaussian c.m. momentum distribution with width measured in electron scattering [31]. An independent measurement of the pair c.m. momentum distribution is given by the ^{10}B momentum distribution (Extended Data Fig. 6e-h) that is measured here for the first time and is also consistent with the GCF predictions.

Last we examine the factorization of the measured SRC pairs from the the residual nuclear system. The strong two-body interaction between the nucleons in the pair was predicted [13, 16] to allow modeling its distribution as independent functions of the pair relative and c.m. motion, with no correlation between them. Such factorization dramatically simplifies SRC calculations and should be evident experimentally by a lack of correlation between the pair c.m. and relative momenta.

Figure 5b shows the distribution of the cosine of the angle between the ^{10}B fragment momentum (i. e. pair c.m. momentum) and the pair relative momentum given by $\mathbf{p}_{\rm rel} = (\mathbf{p}_{\rm miss} - \mathbf{p}_n)/2$, where $\mathbf{p}_n$ is the reconstructed recoil neutron momenta. The GCF assumes the above mentioned factorization and therefore predicts a flat distribution. The data is consistent with this asumption. Therefore by reporting here on the first measurement of SRC pairs with the detection of the residual bound $A-2$ nucleons system we are able to provide first experimental evidence for the factorization of SRC pairs from the many-body nuclear medium.

Conclusions

The dominant contributions of ISI/FSI to nucleon-knockout scattering measurements has been a major difficulty for experimentally extracting nucleon distributions in nuclei [13, 32–35]. Even in high-energy electron scattering at selected kinematics that minimize their contributions, the remaining FSI effect had to be taken into account using theoretical estimates that introduce significant model dependence to the obtained results [3, 13, 14, 35, 36].

At lower beam energies, the method of quasi-free proton-induced nucleon knockout in inverse kinematics

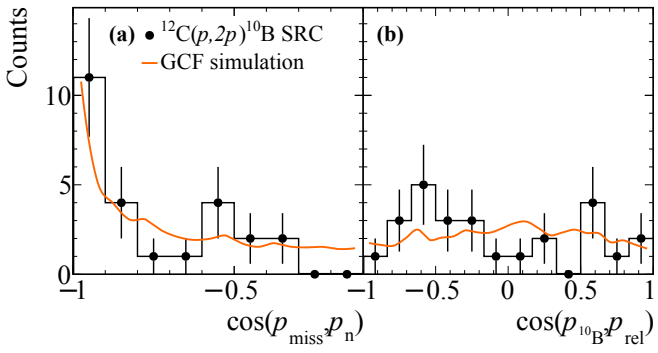

Fig. 5. | Angular correlations in SRC breakup events. Distributions of the cosine of the angle between (a) the recoil nucleon and missing momentum and (b) ^{10}B fragment and pair relative-momentum. Data (black points) are compared with GCF predictions (orange lines). Data error bars show statistical uncertainties assuming poisson distribution at the 1σ confidence level.

has been recently developed and applied to study the single-particle structure of exotic nuclei [4, 5, 8, 25]. The data analysis and interpretation of these results heavily relies on the assumption that the extracted particle distributions are free from FSI contamination that has not been experimentally proven to date.

Our findings however clearly demonstrate the feasibility of accessing properties of single-nucleons and SRC nucleon pairs in neutron-rich nuclei using high-energy radioactive beams, produced at upcoming accelerator facilities such as FRIB and FAIR. With this method, we accomplished a big step towards realizing the goal of such facilities, which is exploring the formation of visible matter in the universe in the laboratory. The presented experimental method thus provides a basis to approximate, as closely as possible, the dense cold neutron-rich matter in neutron stars in the laboratory.

[1] J. Kelly, Adv. Nucl. Phys. **23**, 75 (1996).
[2] L. Lapikas, Nuclear Physics A **553**, 297 (1993).
[3] D. Rohe *et al.* (E97-006 Collaboration), Phys. Rev. Lett. **93**, 182501 (2004).
[4] T. Kobayashi *et al.*, Nucl. Phys. A **805**, 431 (2008).
[5] T. Wakasa, K. Ogata, and T. Noro, Prog. Part. Nucl. Phys. **96**, 32 (2017).
[6] A. Gade *et al.*, Phys. Rev. C **77**, 044306 (2008).
[7] J. Tostevin and A. Gade, Phys. Rev. C **90**, 057602 (2014), arXiv:1409.6576 [nucl-th].
[8] L. Atar *et al.*, Phys. Rev. Lett. **120**, 052501 (2018).
[9] A. Schmidt *et al.* (CLAS), Nature **578**, 540 (2020), arXiv:2004.11221 [nucl-ex].
[10] G. Jacob and T. Maris, Rev. Mod. Phys. **38**, 121 (1966).
[11] P. Hansen and J. Tostevin, Ann. Rev. Nucl. Part. Sci. **53**, 219 (2003).
[12] W. Cosyn and J. Ryckebusch, Phys. Rev. C **80**, 011602 (2009), arXiv:0904.0914 [nucl-th].
[13] C. Ciofi degli Atti, Phys. Rept. **590**, 1 (2015).
[14] O. Hen, G. A. Miller, E. Piasetzky, and L. B. Weinstein, Rev. Mod. Phys. **89**, 045002 (2017).
[15] H. Feldmeier, W. Horiuchi, T. Neff, and Y. Suzuki, Phys. Rev. C **84**, 054003 (2011), arXiv:1107.4956 [nucl-th].
[16] R. Cruz-Torres, D. Lonardoni, R. Weiss, N. Barnea, D. W. Higinbotham, E. Piasetzky, A. Schmidt, L. B. Weinstein, R. B. Wiringa, and O. Hen, arXiv (2019), arXiv:1907.03658 [nucl-th].
[17] P. Spiller and G. Franchetti, Nucl. Instrum. Meth. A **561**, 305 (2006).
[18] "Frib400: The scientific case for the 400 mev/u energy upgrade of frib," https://frib.msu.edu/_files/pdfs/frib400_final.pdf (2019).
[19] B. Mukherjee, P. B. Patel, Z. Yan, R. J. Fletcher, J. Struck, and M. W. Zwierlein, Phys. Rev. Lett. **122**, 203402 (2019).
[20] I. Bloch, J. Dalibard, and W. Zwerger, Rev. Mod. Phys. **80**, 885 (2008).
[21] R. Cruz-Torres *et al.* (Jefferson Lab Hall A Tritium), Phys. Rev. Lett. **124**, 212501 (2020), arXiv:2001.07230 [nucl-ex].
[22] J.-W. Chen, W. Detmold, J. E. Lynn, and A. Schwenk, Phys. Rev. Lett. **119**, 262502 (2017), arXiv:1607.03065 [hep-ph].
[23] J. Lynn, D. Lonardoni, J. Carlson, J. Chen, W. Detmold, S. Gandolfi, and A. Schwenk, J. Phys. G **47**, 045109 (2020), arXiv:1903.12587 [nucl-th].
[24] A. Obertelli and T. Uesaka, Eur. Phys. J. A **47**, 105 (2011), arXiv:1109.5091 [nucl-ex].
[25] V. Panin *et al.*, Phys. Lett. B **753**, 204 (2016).
[26] E. Piasetzky, M. Sargsian, L. Frankfurt, M. Strikman, and J. W. Watson, Phys. Rev. Lett. **97**, 162504 (2006).
[27] R. Subedi *et al.*, Science **320**, 1476 (2008), arXiv:0908.1514 [nucl-ex].
[28] I. Korover, N. Muangma, O. Hen, *et al.*, Phys. Rev. Lett. **113**, 022501 (2014).
[29] O. Hen *et al.*, Science **346**, 614 (2014), arXiv:1412.0138 [nucl-ex].
[30] M. Duer *et al.* (CLAS Collaboration), Phys. Rev. Lett. **122**, 172502 (2019), arXiv:1810.05343 [nucl-ex].
[31] E. O. Cohen *et al.* (CLAS Collaboration), Phys. Rev. Lett. **121**, 092501 (2018), arXiv:1805.01981 [nucl-ex].
[32] I. Bobeldijk *et al.*, Phys. Rev. Lett. **73**, 2684 (1994).
[33] K. I. Blomqvist *et al.*, Phys. Lett. **B421**, 71 (1998).
[34] J. van Leeuwe, W. Hesselink, E. Jans, W. Kasdorp, J. Laget, C. Onderwater, A. Pellegrino, and J. Templon, Phys. Lett. B **523**, 6 (2001).
[35] F. Benmokhtar *et al.* (Jefferson Lab Hall A), Phys. Rev. Lett. **94**, 082305 (2005), arXiv:nucl-ex/0408015.
[36] L. Frankfurt, M. Sargsian, and M. Strikman, Int. J. Mod. Phys. A **23**, 2991 (2008), arXiv:0806.4412 [nucl-th].
[37] V. Kekelidze, A. Kovalenko, R. Lednicky, V. Matveev, I. Meshkov, A. Sorin, and G. Trubnikov, Nucl. Phys. A **904-905**, 945c (2013).
[38] N. N. A. et al., in *Cryogenics 2019. Proceedings of the 15th IIR International Conference: Prague, Czech Republic, April 8-11, 2019.* (2019).
[39] T. Aumann, C. Bertulani, and J. Ryckebusch, Phys. Rev. C **88**, 064610 (2013), arXiv:1311.6734 [nucl-th].
[40] M. Hussein, R. Rego, and C. Bertulani, Phys. Rept. **201**, 279 (1991).
[41] A. Ozawa, T. Suzuki, and I. Tanihata, Nucl. Phys. A **693**, 32 (2001).
[42] G. Alkhazov, S. Belostotsky, and A. Vorobev, Phys. Rept. **42**, 89 (1978).
[43] M. Kapishin (BM@N), Nucl. Phys. A **982**, 967 (2019).
[44] "Conceptual design report bm@n — baryonic matter at nuclotron," ().
[45] S. Khabarov, E. Kulish, V. Lenivenko, A. Makankin, A. Maksymchuk, V. Palichik, M. Patsyuk, S. Vasiliev, A. Vishnevskij, and N. Voytishin, EPJ Web Conf. **201**, 04002 (2019).
[46] Y. Kovalev, M. Kapishin, S. Khabarov, A. Shafronovskaia, O. Tarasov, A. Makankin, N. Zamiatin, and E. Zubarev, Journal of Instrumentation **12**, C07031 (2017).
[47] V. Babkin *et al.*, Nucl. Instrum. Meth. A **824**, 490 (2016).
[48] "Bm@n daq system," ().
[49] "Root cern: Multi-dimensional fit," https://root.cern.ch/doc/master/classTMultiDimFit.html.

Acknowledgments We acknowledge the efforts of the staff of the Accelerator and High-Energy Physics Divisions at JINR that made this experiment possible. The

research was supported by the Israel Science Foundation, the Pazi Foundation, the BMBF under grant ..., the DFG under grant, the TU Darmstadt-GSI cooperation, RFBR grant number 18-02-40046, 18-02-40084\19 ..... .

Author Contributions The experimental set up at the Nuclotron was designed and constructed by the BM@N Collaboration at JINR. The design and construction of the TAS was led by G.L., who also led the data taking period. Data acquisition, processing and calibration, Monte Carlo simulations of the detector and data analyses were performed by a large number of BM@N Collaboration members, who also discussed and approved the scientific results. M.R. contributed to the RPC analysis, V.P. contributed to the Si/MWPC analysis, D.B. contributed to the GEM analysis, and N.V. contributed to the DCH analysis. The entire analysis was done by J.K., M.P., V.L., E.P.S., T.A., G.J., V.P., and M.D., with input from O.H., E.P., T.A., M.K. and A.C., and reviewed by the BM@N collaboration.

Full Author List

M. Patsyuk,[1,2] J. Kahlbow,[1,3] G. Laskaris,[1,3] M. Duer,[4] V. Lenivenko,[2] E. P. Segarra,[1] T. Atovullaev,[2,23] G. Johansson,[3] T. Aumann,[4,6,7] A. Corsi,[5] O. Hen,[1] M. Kapishin,[2] V. Panin,[5,6] E. Piasetzky,[3] Kh. Abraamyan, [2] S. Afanasiev, [2] G. Agakishiev, [2] E. Aleksandrov, [2] I. Aleksandrov, [2] P. Alekseev, [9] K. Alishina, [2] D. Alvear-Terrero,[21] E. Atkin, [11] T. Aushev,[12] V. Babkin,[2] V. Balandin, [2] N. Balashov, [2] A. Baranov, [14] D. Baranov, [2] A. Baranov, [13] N. Baranova, [13] N. Barbashina, [11] P. Batyuk, [2] D. Baznat, [20] M. Baznat, [20] S. Bazylev, [2] A. Beck, [3] C. A. Bertulani, [25] D. Blaschke, [21] D. Blau, [10] G. Bogdanova, [13] D. Bogoslovsky, [2] A. Bolozdynya, [11] E. Boos, [13] K. Boretzky, [6] Y. T. Borzunov, [2] V. Burtsev, [2] M. Buryakov, [2] S. Buzin[2] A. Chebotov,[2] J. Chen, [16] P. Chudoba, [21] A. Ciszewski, [21] R. Cruz-Torres,[1] B. Dabrowska,[2] D. Dabrowski, [22] D. Dementev, [2] A. Dmitriev, [2] Z. Deng, [17] A. Dryuk, [14] A. Dryablov, [2] P. Dulov,[2] D. Egorov, [2] V. Elsha,[2] A. Fedunin, [2] I. Filippov, [2] K. Filippov, [11] I. Filozova, [2] D. Finogeev,[14] I. Gabdrakhmanov, [2] A. Galavanov, [11] I. Gasparic, [24,4] O. Gavrischuk, [2] D. Gerasimov, [14] K. Gertsenberger, [2] A. Gillibert, [13] V. Golovatyuk, [2] M. Golubeva, [14] F. Guber,[14] B. Guo,[17] D. Han, [17] Yu. Ivanova, [2] A. Ivashkin, [14] A. Izvestnyy,[14] V. Kabadzhov, [15] S. Kakurin, [2] V. Karjavin, [2] D. Karmanov, [13] N. Karpushkin, [14] G. Kasprowicz, [22] R. Kattabekov, [2] V. Kekelidze, [2] S. Khabarov, [2] P. Kharlamov, [13] A. Khvorostukhin, [20] D. Kirin, [9] Yu. Kiryushin, [2] A. Kisiel, [22] P. Klimai, [12] D. I. Klimanskiy, [2] V. Kolesnikov, [2] A. Kolozhvari, [2] A. V. Konstantinov, [2] Yu. Kopylov, [2] M. Korolev, [13] I. Korover, [3] L. Kovachev, [15] A. Kovalenko, [2] I. Kovalev, [13] Yu. Kovalev, [2] I. Kudryashov, [13] A. Kugler, [18] S. Kuklin, [2] V. Kukulin, [13] E. Kulish, [2] A. Kurganov, [13] S. Kushpil, [18] V. Kushpil, [18] A. Kuznetsov[2] E. Ladygin, [2] D. Lanskoy, [13] I. Larin, [9] N. Lashmanov, [2] M. Ławryńczk, [22] R. Lewandkow, [21] Y. Li, [17] V. Leontiev, [13] M. Linczuk, [22] E. Litvinenko, [2] S. Lobastov, [2] B. Löher,[6,4] Y. G. Ma, [16] A. Makankin, [2] A. Makarov, [14] A. Makhnev, [14] A. Maksymchyuk, [2] A. Malakhov, [2] I. Mardor, [3] M. Merkin, [13] S. Merts, [2] H. Miao, [17] V. Mikhailov, [18] A. Morozov, [2] S. Morozov, [14] Yu. Murin, [2] G. Musulmanbekov,[2] R. Nagdasev, [2] S. Nemnyugin, [14] D. Nikitin,[2] D. Oleynik,[2] V. Palchik, [2] A. Petrosyan, [2] Ia. Panasenko, [19] D. Peresunko, [10] M. Peryt, [22] O. Petukhov, [14] Yu. Petukhov, [2] S. Piyadin, [2] S. Plamowski, [22] M. Platonova, [13] V. Plotnikov, [2] J. Pluta, [22] D. Podgainy, [2] G. Pokatashkin, [2] Yu. Potrebenikov, [2] K. Poźniak,[22] A. Reshetin, [14] O. Rogachevsky, [2] V. Rogov, [2] P. Rokita, [22] R. Romaniuk, [22] K. Rosłon, [22] D. Rossi, [4] V. Roudnev, [14] I. Rufanov, [2] P. Rukoyatkin, [2] M. Rumyantsev [2] D. Sakulin, [2] V. Samsonov, [11] H. Scheit, [4] A. Schmidt,[1] H. R. Schmidt, [19] A. Sedrakian, [21] S. Sedykh, [2] I. Selyuzhenkov, [11] V. Semyachkin, [9] P. Senger, [11] S. Sergeev, [2] C. Shen, [17] A. Sheremetev, [2] A. Sheremeteva, [2] A. Shipunov, [2] M. Shitenkov, [2] M. Shopova, [15] V. Shumikhin, [11] A. Shutov, [2] V. Shutov, [2] H. Simon, [6] I. Slepnev, [2] V. Slepnev, [2] I. Slepov, [2] A. Solomin, [13] A. Sorin, [2] V. Sosnovtsev, [11] V. Spaskov, [2] T. Starecki, [22] A. Stavinskiy, [9] M. Stepanova, [14] E. Streletskaya, [2] O. Streltsova, [2] M. Strikhanov, [11] N. Sukhov, [2] D. Suvarieva,[2] J. Tanaka, [4] A. Taranenko, [11] N. Tarasov, [2] O. Tarasov, [2] V. Tarasov, [9] A. Terletsky, [2] O. Teryaev, [2] V. Tcholakov, [15] V. Tikhomirov, [2] A. Timoshenko, [2] N. Topilin, [2] B. Topko, [2] H. Törnqvist, [4] T. Traczyk, [22] T. Tretyakova, [13] I. Tyapkin [2] V. Vasendina, [2] A. Vishnevsky, [2] V. Volkov, [13] E. Volkova, [19] A. Voronin, [2] A. Voronin, [13] N. Voytishin, [2] V. Wagner, [4] Yi. Wang, [17] O. Warmusz, [21] P. Wieczorek, [22] D. Wielanek,[22] Z. Xiao,[17] Z. Xu, [17] I. Yaron, [3] V. Yurevich, [2] W. Zabołotny,[22] N. Zamiatin, [2] M. Zavertiaev, [2] S. Zhang, [16] E. Zherebtsova, [14] V. Zhezher, [2] N. Zhigareva, [9] X. Zhu, [17] P. Zhuang,[17] A. Zinchenko, [2] Z. Zou, [17] E. Zubarev, [2] M. Zuev[2]

[1] Massachusetts Institute of Technology, Cambridge, Massachusetts 02139, USA. [2] Joint Institute for Nuclear Research, Dubna 141980, Russia. [3] School of Physics and Astronomy, Tel Aviv University, Tel Aviv 69978, Israel. [4] Institut für Kernphysik, Technische Universität Darmstadt, 64289 Darmstadt, Germany. [5] IRFU, CEA, Université Paris-Saclay, F-91191 Gif-sur-Yvette, France. [6] GSI Helmholtzzentrum für Schwerionenforschung GmbH, Planckstr. 1, 64291 Darmstadt, Germany. [7] Helmholtz Forschungsakademie Hessen für FAIR, Max-von-Laue-Str. 12, 60438 Frankfurt, Germany. [8] Institute for Nuclear Research of the RAS (INR RAS), Moscow, Russia. [9] Institute for Theoretical and Experimental Physics (ITEP), Moscow, Russia. [10] Kurchatov Institute, Moscow. [11] National Research Nuclear

University MEPhI, Moscow, Russia. [12] Moscow Institute of Physics and Technology (MIPT), Moscow, Russia. [13] Skobeltsyn Institute of Nuclear Physics, Moscow State University (SINP MSU), Moscow, Russia. [14] St Petersburg University (SPbU), St Petersburg, Russia. [15] Plovdiv University "Paisii Hilendarski", Plovdiv, Bulgaria. [16] Fudan University, Shanghai, China. [17] Tsinghua University, Beijing, China. [18] Nuclear Physics Institute, CAS, Řež, Czech Republic. [19] University of Tübingen, Tübingen, Germany. [20] Institute of Applied Physics, ASM, Chisinau, Moldova. [21] University of Wroclaw, Wroclaw, Poland. [22] Warsaw University of Technology, Warsaw, Poland. [23] Dubna State University, Dubna 141980, Russia. [24] Rudjer Boskovic Institute, Zagreb, Croatia. [25] Texas A&M University-Commerce, Commerce, Texas 75429, USA.

Methods

Ion Beam. The primary beam ions were produced in a Creon source and accelerated in the Nuclotron [37]. delivered quasi-continuously in 2 second long pulses with a 8 second pause between pulses. Each pulse delivered 2.5×10^5 ions on average.

The beam contained a mixture of Carbon-12, Nitrogen-14, and Oxygen-16 ions with fractions of 68%, 18%, and 14% respectively. The ^{12}C ions have a beam momentum of 3.98 GeV/c/u at the center of the LH_2 target. They are focused on the target with a beam diameter of about 4 cm, See Extended Data Fig. 1c.

The beam ions are identified on an event-by-event basis using their energy loss in the BC detectors (BC1, BC2 upstream the target) that is proportional to their nuclear charge squared Z^2. The selection of the incoming nuclear species is shown in Extended Data Fig. 8. Pile-up events are rejected by checking the multiplicity of the BC2 time signal.

The detectors upstream the target. Prior to hitting the target the beam was monitored by the two thin scintillator-based beam counters (BC1, BC2) and two multi-wire proportional chambers (MWPCs) mentioned above. The MWPCs determined the incident beam ion trajectory for each event. Besides using the energy deposition in the BCs for particle identification, the BC closer to the target was readout by a fast MCP-PMT used to define the event start time t_0. Beam halo interactions were suppressed using a dedicated BC veto counter (V-BC), consisting of a scintillator with a 5 cm diameter hole in its center.

Liquid-hydrogen target. The target [38] was cryogenically cooled and the hydrogen was recondensated using liquid helium. The liquid hydrogen was held in a 30 cm long and 6 cm diameter aluminized Mylar cylindrical container at 20 Kelvin and 1.1 atmospheres. The container entrance and exit windows were made out of 110 micron thick Mylar. The target constitute a 14% interaction length for ^{12}C. A sketch of the target cell is shown in Extended Data Fig. 1.

Two-arm spectrometer (TAS). A two-arm spectrometer was placed downstream of the target and was used to detect the two protons from the $(p, 2p)$ reaction that emerge at $24^\circ - 37^\circ$. The vertical acceptance of each arm equals $\pm 7^\circ$. These laboratory scattering angles correspond to $\sim 90^\circ$ (75° to 101°) QE scattering in the two-protons center-of-mass (c.m.). Each spectrometer arm consisted of scintillator trigger counters (TC), gas electron multiplier (GEM) stations, and multi-gap resistive plate chamber (RPC) walls.

Proton tracks are formed using their hit location in the GEM and RPC walls. These allow determining the scattered protons angles relative to the incident beam direction. The vertex resolution along the beam-line direction is 1.8 cm (1σ) and was measured using a triple-foil lead target as detailed in the Online Supplementary Material.

The time difference between the RPC and t_0 signals define the proton time of flight (TOF) that, combined with the measured track length, is used to determine its momentum. Measurements of gamma rays from interactions with a single-foil lead target were used for absolute time-of-flight calibration and determine a resolution of better 100 ps with respect to t_0 (for a total TOF resolution of 175 ps). The obtained TOF resolution dominate the momentum resolution, see online Supplementary Materials for details.

Data Taking and Quality. Signals from the TAS-TCs were combined with the BC and V-BC scintillators signals to form the main $^{12}C(p, 2p)$ reaction trigger for the experiment. Additional triggers were set up for monitoring and calibration purposes, see online Supplementary Materials for details.

The stability of the trigger was monitored on-line during the experiment as part of our data quality control. We collected and recorded about 20 million triggers. The ratio between BC2/BC1 and BC4/BC3 was not smaller than 65%, and the rate on the V-BC is on average 24% relative to BC2. The physics data were taken with a rate of about 180 Hz as measured during a beam pulse duration. Variations of beam detector pulse height over the measurement time was monitored and accounted for in the analysis. No significant run-to-run variations were observed in any of the final observables.

Reaction Vertex and Proton Identification. The z-position (along the beamline) of the reaction vertex is reconstructed from two tracks in the TAS, while the (x, y) position is obtained from the extrapolated MWPC track in front of the target since this system provides a better transverse position resolution. Details about the algorithm and performance can be found in the Online Supplementary Materials.

The reconstructed vertex position along the beam-line and transverse to it with the liquid-hydrogen target inserted is shown in Extended Data Fig. 1. Clearly, the structure of the target is reconstructed, including the LH_2 volume but also scattering from other in-beam materials such as the target walls, styrofoam cover, and various isolation foils. The vertex quality is ensured by requiring that the minimum distance between the two tracks, which define the vertex, is smaller than 4 cm. In addition, we place a selection on the absolute z-vertex requiring it to be reconstracted within ± 13 cm from the center of the target.

Scattering from the target vessel that was not rejected by the veto counter is removed by a cut on the (x, y)-

vertex direction, excluding the strong peak at the entrance of the target (Extended Data Fig. 1c).

Having determined the tracks and the vertex, the momenta of the presuming two protons are calculated with respect to the incoming beam direction and using the time-of-flight information between the target and the RPC.

In order to select $(p, 2p)$ events from Quasi-Free Scattering (QFS), other particles that also create a track but originating from e. g. inelastic reactions like pions need to be rejected. We apply several criteria, that are further outlined in the next section, but the basic selection is applied to the velocity of the two measured particles which is shown in Supplementary Material Fig. 4a. In the analysis, every particle must pass the velocity condition $0.8 < \beta < 0.96$ that removes fast and slow pions in coincidence with another particle.

Fragment Detection. Nuclear fragments following the $(p, 2p)$ reaction are emitted at small angles with respect to the incident beam with momentum that is similar to the beam momentum. Three silicon (Si) planes and two MWPCs are placed in the beam-line downstream the target to measure the fragment scattering angle. Following the MWPCs the fragments enter a large acceptance 2.87 T·m dipole magnet, and are bent according to their momentum-to-charge ratio (P/Z), i. e. magnetic rigidity. Following the magnet, two drift chambers (DCH) with 8 wire-planes each are used to measure the fragment trajectory.

The fragment momenta are determined from the measurement of their bending angle in the magnet. Fragment identification (nuclear mass and charge) is done using their bend in the magnetic field and energy deposition in two scintillator BCs (3,4) placed between the target and the magnet entrance, see Fig. 1b. The latter is proportional to the sum over all fragment charges squared, $Z_{\text{eff}} \equiv \sqrt{\sum Z^2}$.

Fragment Momentum and Identification. We follow a simulation-based approach to derive P/Z from a multi-dimensional fit (MDF) to the measured fragment trajectories before and after the magnet. The particle trajectory is determined using the MWPC-Si tracking system before the magnet, and using the DCHs after the magnet. Both tracks serve as input for the P/Z determination.

The momentum resolution was determined using empty target measurements of ^{12}C ions and found to equal 0.7 GeV/c (1.5%) (Supplementary Fig. 2). This resolution is consistent with the resolution expected from events obtained with simulation that accounts for the incoming beam energy spread. The achieved momentum accuracy is evaluated to equal 0.2%. Using our beam trigger (see online Supplementary) we verified that the momentum reconstruction resolution is the same when the ^{12}C ions go through a full liquid-hydrogen target.

The fragment tracking efficiency, including the detection efficiency of the upstream MWPC-Si, downstream DCH detectors, and track reconstruction algorithm equals $\sim 50\%$. See online Supplementary Materials for details on the tracking algorithms and its performance.

Figure 1b illustrates an example of this fragment identification from the experimental data using P/Z obtained by the MDF vs. total charge measured in the scintillators.

This work focuses only on fragments with nuclear charge of 4 or larger with a single track matched between the upstream and downstream tracks. Therefore, although the charge of the fragments is only measured as integrated signal in BC3 and BC4 counters, the Boron isotopes can be selected unambiguously since no possible combination of fragments could otherwise mimic a signal amplitude proportional to $\sum Z^2 = 25$. In the case of ^{10}Be, the only other fragment of interest here with $Z_{\text{eff}} = 4$, contamination from within the resolution is excluded by using the additional P/Z information. ^{10}Be is the only possible fragment with $P/Z \sim 10$ GeV/c in that region and is well separated.

Besides requesting a good vertex and single global-track events, we employ Z_{eff} and P/Z selection criteria to identify ^{11}B, ^{10}B, or ^{10}Be. A two-dimensional charge selection, as for the incoming charge, was applied here for BC3 and BC4. A two-dimensional selection in P/Z vs. Z_{eff} was also applied as shown in Fig. 1b with a 2σ selection.

Single heavy fragment detection efficiencies. As discussed above, this work is limited to reactions with a single heavy ($Z \geq 4$) fragment in the final state. The detection of such a fragment depends on the ability of the fragment to emerge from the liquid hydrogen target without re-interacting, and our ability to identify its charge in the two BCs downstream of the target, and reconstruct its tracks before and after the magnet.

We extract the efficiencies for the charge and track reconstruction using data collected with a beam and no target. We assume that within the quoted uncertainties below, there is no difference between the efficiencies for detecting $Z = 6$ and $Z = 4$ and 5 fragments.

The charge determination efficiency in the BCs downstream the target was determined by selecting incident ^{12}C ions based on their energy loss in the BC1 and BC2 counters (see Extended Data Fig 8). We then examine the fraction of those ^{12}C ions also identified by their energy loss in BC3 and BC4 downstream the target. This fraction defines a charge identification efficiency of $\epsilon_Z = (83 \pm 6)\%$, where the uncertainty is obtained from examining different energy-deposition cuts between $2 - 3\sigma$ on the Gaussian distribution in BC3 and BC4.

The standard deviation in efficiency from this cut variation relative to the mean value defines the uncertainty. The fraction of such $Z_{\rm in} = Z_{\rm out} = 6$ events with a single reconstructed track and $P/Z = 8$ GeV/c is equal to $(50 \pm 5)\%$. In case of ^{10}Be fragments the tracking efficiency is $(50 \pm 15)\%$ due to larger systematic effects. More details are given below in "Extracting QE ratios" and in the online Supplementary.

Single-Proton Knockout Data-Analysis. The basic selection criteria for any analysis require an incoming ^{12}C, as well as a good reaction vertex, while the particles in the arms pass the velocity condition. These selections criteria define the inclusive $(p, 2p)$ reaction channel, which is dominated by FSI and IE scattering. The exclusive reaction channel requires the additional detection of a ^{11}B fragment, with a single global-track condition and defines the one-proton QFS, that includes both QE and IE scattering.

We select a bound ^{11}B where the $3/2^-$ ground-state is populated with the largest cross section. However, we cannot distinguish bound excited states that de-excite via γ-ray emission that are also populated in our experiment. Previous works [25] found the contribution from such states to be small, coming primarily from the $1/2^-$ and $3/2^-$ states that contribute $\sim$10% each to the total cross section. This contribution also correspond to p-shell knockout and does not impact the resulting momentum distribution significantly.

In order to identify real $(p, 2p)$ QE events and reject IE events, we chose missing energy and the in-plane opening angle of the two particles measured in the arms, looking at quantities that are reconstructed from that independent detection system. An elliptical cut denoted by $2\,\sigma$ is applied in each direction (Fig. 2). The standard deviation was obtained from a Gaussian fit to $E_{\rm miss}$ ($\sigma = 0.108$ GeV) and $\theta_{p1} + \theta_{p2}$ ($\sigma = 1.8^\circ$).

The missing energy is defined as $E_{\rm miss} = m_p - e_{\rm miss}$, where $e_{\rm miss}$ is the energy component of $\bar{p}_{\rm miss}$ in the rest frame of the ^{12}C nucleus. The boost from the laboratory system into the rest frame is applied along the incoming-beam direction considering the reduced beam energy at the reaction vertex. The selection region for QE events is defined in the exclusive channel with fragment selection, in a 2σ ellipse as indicated in Fig. 2. The IE part is defined from the remaining events within the other ellipse. The same criteria are applied in the inclusive channel. Correlations with other kinematical variables are shown in Extended Data Fig. 9.

The $M^2_{\rm miss}$ spectrum in Extended Data Fig. 2a shows the squared missing mass for the exclusive channel before and after applying the QE cut, clearly showing that we select background-free QE events with a missing mass that equals the proton mass. A lower boundary in the squared missing mass of $M^2_{\rm miss} > 0.47$ GeV$^2/c^4$ is applied. Since the chosen selection criteria might influence other kinematical variables of $\bar{p}_{\rm miss}$ (Eq. 2), we show the momentum distributions and angular correlations with less strict selection in the Extended Data (Figs. 2, 3) which do not show a different behavior and are also described well by the simulation.

Single-Proton Knockout Simulation. We compare the quasielastic ^{12}C$(p, 2p)^{11}$B data to a MonteCarlo simulation for the proton quasielastic scattering off a moving ^{12}C. In the calculation, the ^{12}C system is treated as spectator plus initial proton, $\mathbf{p}_{^{12}\rm C} = \mathbf{p}_{^{11}\rm B} + \mathbf{p}_i$. The proton's initial momentum distribution in ^{12}C is sampled from a theoretical distribution. Note that all kinematical quantities discussed here correspond to the carbon rest-frame.

The momentum distributions are calculated in the eikonal formalism for quasi-free scattering as described in Ref. [39]. In this work we compare the data to the momentum-distribution calculated without absorption effects, i. e. without multiple-scattering. Here we also compare to the same calculation that includes absorption effects from the imaginary part of the potential explicitly, calculated in the optical limit of Glauber theory. See in Extended Data Fig. 10.

The distorted waves are calculated from the real and imaginary part of the optical potential for the interaction between proton and nucleus. The single particle wave function of the removed proton is generated from a Woods-Saxon potential with radius given by $R = 1.2 \cdot A^{1/3}$ fm and diffuseness $a = 0.65$ fm, while the depth of the potential was adjusted to reproduce the removal energy, $S_p = 15.96$ MeV, of a proton from the $p_{3/2}$-shell. For the ^{12}C nucleus a density distribution from electron scattering was used as input, assuming that is has the same profile for the proton and neutron densities. The density is of the form $\rho_{^{12}\rm C} = (1+\alpha\cdot(r/b)^2)\cdot\exp\left\{-r^2/b^2\right\}$, with $\alpha = 1.4$ and b chosen so as to reproduce the RMS radius of the ^{12}C, $b = 2.47$ fm.

Although the fragment selection removes events from FSI and we do not need to account for their scattering into measured phase space, we look at the calculation with absorption since the survival probability is larger if the knockout happens at the nuclear surface. This effect might create a difference from no distortions. However, the momentum distributions with and without absorption look very similar, see Ext. Data Fig. 10, and do not seem to have a large impact on the reconstructed initial momentum distribution in a light system such as ^{12}C.

In terms of the kinematics, we raffle $|\mathbf{p}_i|$ from the total-momentum distribution and randomize its direction. The proton's off-shell mass is

$$m^2_{\rm off} = m^2_{^{12}\rm C} + m^2_{^{11}\rm B} - 2m_{^{12}\rm C} \cdot \sqrt{m^2_{^{11}\rm B} + \mathbf{p}^2_i}. \quad (3)$$

The two-body scattering between the proton in ^{12}C and the target proton is examined in their c.m. frame. The elastic-scattering cross section is parameterized from free

pp differential cross section data. Following the scattering process, the two protons and ^{11}B four-momenta are boosted back into the laboratory frame.

The two-arm spectrometer was placed such that it covers the symmetric, large-momentum transfer, 90° c.m. scattering region. Given the large forward momentum, the detectors cover an angular acceptance of $\sim 24^\circ < \theta < 37^\circ$ in the laboratory system which corresponds to $\sim 75^\circ < \theta_{\rm c.m.} < 101^\circ$ in the c.m. frame.

In order to compare the simulated data to the experimental distributions, the simulation is treated and analyzed in the same way as the experimental data. Experimental acceptances are included. Resolution effects are convoluted to proton and fragment momenta. The proton time-of-flight resolution ΔToF/ToF is 0.95% at 2 GeV/c and the angular resolution 5 mrad, while the fragment momentum resolution is 1.5% and the angular resolution 1.1 mrad in the x and y directions. The angular resolution of the incoming beam is 1.1 mrad. The beam-momentum uncertainty, examined as Gaussian profile, does not significantly impact rest-frame momentum distribution as long as the nominal beam momentum is the same used for extracting physical quantities (or observables) from the experimental data and the simulated ion. However, the momentum distributions are dominated by the width of the input p-shell momentum distribution. When comparing, the simulation is normalized to the integral of the experimental distributions. We find overall good agreement between experiment and Monte Carlo simulation showing that the reaction mechanism and QE events sample the proton's initial momentum distribution in ^{12}C. Additional data-simulation comparison are shown in Extended Data Fig. 3.

Extracting QE ^{12}C$(p,2pX)/^{12}$C$(p,2p)$ ratios for ^{11}B, ^{10}B, and ^{10}Be. To extract the fraction of $(p,2p)$ events with a detected heavy fragment we need to apply several corrections to the number of measured events which do not cancel in the ratio. The ratio of the exclusive cross section with a detected fragment to the inclusive cross section is given by:

$$\frac{^{12}\mathrm{C}(p,2p)\mathrm{X}}{^{12}\mathrm{C}(p,2p)} = \frac{R}{\epsilon_Z \times \epsilon_{\rm track} \times att}, \qquad (4)$$

where

- R is the measured ratio based on the number of QE events for each sample. We added a cut on low missing momentum, $p_{\rm miss} < 250$ MeV/c, in addition to the missing energy and in-plane opening angle cuts to clean up the inclusive $(p,2p)$ sample, and focusing at the region of small missing momentum.
- ϵ_Z is the outgoing fragment charge efficiency. We consider a value of $\epsilon_Z = (83 \pm 6)\%$, see discussion above.
- $\epsilon_{\rm track}$ is the outgoing fragment tacking efficiency. We consider a value of $\epsilon_{\rm track} = (50 \pm 5)\%$ for ^{11,10}B, and $\epsilon_{\rm track} = (50 \pm 15)\%$ for ^{10}Be, see discussion above.
- att is the attenuation of the outgoing fragment due to secondary fragmentation in the target. After the reaction, the flux of the fragment depends on the remaining distance the fragment needs to travel in the target. The attenuation is given by the reduction of this flux

$$att = \exp(-\rho\sigma_{\rm tot} z), \qquad (5)$$

where ρ is the target density and $\sigma_{\rm tot}$ the total reaction cross section. We evaluate the attenuation factor by taking an average over the 30 cm target length, using $\sigma_{\rm tot} = 220 \pm 10$ mb (assumed to be the same for ^{10}B,^{10}Be within uncertainty), such that $att = 0.87 \pm 0.01$. Additional break-up reactions due to material in the beam-line downstream the target were estimated (and scaled) based on the total cross section on carbon. The contribution to the secondary reaction probability is comparably small, in particular reactions from ^{11}B to ^{10}B or ^{10}Be are negligible.

The total reaction cross section $\sigma_{\rm tot}$ is calculated in eikonal reaction theory [40] using the ^{11}B harmonic-oscillator like density distribution and the NN cross section at 4 GeV/c/u as the input. In a benchmark test it reproduces the measured cross section for ^{11}B+^{12}C at kinetic energy of 950 MeV/u [41] while the beam energy has only a very small impact. We consider the $\sim 5\%$ systematic overestimate of eikonal cross sections compared to measurements as uncertainty.

From Eq. 4 we see that there are four individual contributions to the uncertainty in the ratio of ^{12}C$(p,2pX)/^{12}$C$(p,2p)$: statistics ΔR, efficiencies ($\Delta\epsilon_Z$ and $\Delta\epsilon_{\rm track}$) and attenuation ($\Delta att$). In addition we have a systematic uncertainty due to the event selection cuts. Each event cut was modified over a given σ range and the resulting change in the relative yield was taken as the systematic uncertainty. The 2D $E_{\rm miss}$-angle cuts were varied as $(2 \pm 1/2)\sigma$, where both these quantities are described by a Gaussian. The cut in missing momentum was varied according to the missing momentum resolution like $p_{\rm miss} < 250 \pm 50$ MeV/c. In the following we quote symmetric uncertainties since we did not observed in the simulation a significant asymmetry in the measured quantities. Combining these contributions we obtain the following fractions given with statistical (stat)

and systematic (sys) uncertainties:

$$\frac{^{12}\mathrm{C}(p,2p)^{11}\mathrm{B}}{^{12}\mathrm{C}(p,2p)} = (40.3 \pm 2.0\,(\mathrm{stat}) \pm 5.5\,(\mathrm{sys}))\%,$$
$$\frac{^{12}\mathrm{C}(p,2p)^{10}\mathrm{B}}{^{12}\mathrm{C}(p,2p)} = (11.1 \pm 1.1\,(\mathrm{stat}) \pm 1.5\,(\mathrm{sys}))\%,$$
$$\frac{^{12}\mathrm{C}(p,2p)^{10}\mathrm{Be}}{^{12}\mathrm{C}(p,2p)} = (1.7 \pm 0.4\,(\mathrm{stat}) \pm 0.5\,(\mathrm{sys}))\%.$$

Selecting high-momentum SRC events. We study SRC events by focusing on $^{12}\mathrm{C}(p,2p)^{10}\mathrm{B}$ and $^{12}\mathrm{C}(p,2p)^{10}\mathrm{Be}$ events. We start with the two-proton detection imposing the vertex and β cuts mentioned above. The first cut applied to select SRC breakup events is to look at high-missing momentum, $p_{\mathrm{miss}} > 350$ MeV/c.

The remaining event selection cuts are chosen following a GCF simulation of the $^{12}\mathrm{C}(p,2p)$ scattering reaction off high missing-momentum SRC pairs. After applying the high-missing momentum cut, we look at the in-plane opening angle between the protons for different cases: (a) inclusive $^{12}\mathrm{C}(p,2p)$ events, (b) GCF simulated SRC events, (c) exclusive $^{12}\mathrm{C}(p,2p)^{10}\mathrm{B}$ events, and (d) exclusive $^{12}\mathrm{C}(p,2p)^{10}\mathrm{Be}$ events. The GCF predicts relatively large opening angles that guides our selection of in-plane lab-frame opening angle larger than 63° (that also suppresses contributions from inelastic reactions that contribute mainly at low in-plane angles).

Next we apply a missing-energy cut to further exclude inelastic and FSI contributions that appear at very large missing-energies. To this end we examine the correlation between the missing energy and missing momentum, after applying the in-plane opening angle cut, for the full range of the missing momentum (i. e., without the $p_{\mathrm{miss}} > 350$ GeV/c cut), see Extended Data Fig. 4. We chose to cut on $-110 < E_{\mathrm{miss}} < 240$ MeV.

To improve the selection cuts we use the total energy and momentum conservation in reactions at which we identified a fragment (^{10}B or ^{10}Be). We can write the exclusive missing-momentum in these reactions as

$$\bar{p}_{\mathrm{miss,excl.}} = \bar{p}_{^{12}\mathrm{C}} + \bar{p}_{tg} - \bar{p}_1 - \bar{p}_2 - \bar{p}_{^{10}\mathrm{B(Be)}}. \quad (6)$$

Neglecting the center-of-mass motion of the SRC pair, the missing-mass of this 4-vector should be equal to the nucleon mass $m^2_{\mathrm{miss,excl.}} \backsimeq m^2_N$. The distributions for $^{12}\mathrm{C}(p,2p)^{10}\mathrm{B}$ and $^{12}\mathrm{C}(p,2p)^{10}\mathrm{Be}$ events that pass the missing-momentum, in-plane opening angle, and missing-energy cuts are shown in Extended Data Fig. 5 together with the GCF simulation. To avoid background events with very small values of the missing-mass we choose to cut on $M^2_{\mathrm{miss,excl.}} > 420$ MeV^2/c^4. After applying this cut we are left with 26 $^{12}\mathrm{C}(p,2p)^{10}\mathrm{B}$ and 3 $^{12}\mathrm{C}(p,2p)^{10}\mathrm{Be}$ events that pass all the SRC cuts.

We note that if the measured SRC events were caused by FSI with a neutron in ^{11}B, we would expect to also detect a similar number of ^{10}Be fragments due to FSI with a proton in ^{11}B. At the high energies of our measurement these two FSI processes have almost the same rescattering cross sections [42]. Our measurement of only 3 ^{10}Be events is consistent with the SRC np-dominance expectation and not with FSI.

In addition, while our selection cuts suppress QE scattering events off the tail of the mean-field momentum distribution they do not completely eliminate them. Therefore, some events could result from de-excitation of high-p_{miss} ^{11}B fragments. Using the de-excitation cross-sections of Ref. [25] and the measured number of $^{12}\mathrm{C}(p,2p)^{11}\mathrm{B}$ events that pass our SRC selection cuts (except for the exclusive missing-mass cut), we estimate a maximal background of 4 ^{10}B and 2 ^{10}Be events due to knockout of mean-field protons and subsequent de-excitation.

Characterizing the selected $^{12}\mathrm{C}(p,2p)^{10}\mathrm{B}$ events. The majority of SRC events with a detected fragment comes with ^{10}B. In the Extended Data we present some kinematical distributions of these selected events together with the GCF simulation. Extended Data Fig. 6 shows the total ^{10}B fragment and missing moments as well as their different components. Overall good agreement between the data and simulation is observed.

Due to the high momenta of the nucleons in SRC pairs, it is beneficial to also analyze the missing-momentum distribution in the relativistic light-cone frame where the longitudinal missing-momentum component is given by $\alpha = (E_{\mathrm{miss}} - p^z_{\mathrm{miss}})/m_p$. Similar to p_{miss}, α is calculated in the ^{12}C rest frame where $\hat{z}$ is boosted target-proton direction. $\alpha = 1$ for scattering off standing nucleons. $\alpha < 1$ (> 1) corresponds to interaction with nucleons that move along (against) the beam direction and therefore decrease (increase) the c.m. energy of the reaction $\sqrt{s}$. Extended Data Fig. 7a shows the α distribution for the measured SRC events. We observe that $\alpha < 1$, as predicted by the GCF and expected given the strong s-dependence of the large-angle elementary proton-proton elastic scattering cross-section. for completeness, Extended Data Fig. 7 also shows additional angular correlations between the nucleons in the pair and the ^{10}B fragment, all well reproduced by the GCF.

Estimating the number of SRC $^{12}\mathrm{C}(p,2p)^{10}\mathrm{B}$ and $^{12}\mathrm{C}(p,2p)^{10}\mathrm{Be}$ events. As a consistency check we performed a simple estimate of the expected number of exclusive SRC events based on the measured mean-field $^{12}\mathrm{C}(p,2p)^{11}\mathrm{B}$ event yield. We assume SRCs account for 20% of the wave function [**?**], and that their contribution to the exclusive measurements is suppressed by a factor of 2 as compared to the mean-field $^{12}\mathrm{C}(p,2p)^{11}\mathrm{B}$ due to the transparency of the recoil nucleon [**? ? ?**]. Therefore, we expect a contribution of 11% SRC and 89% mean-field.

The mean-field has contributions leading to bound

states (i. e. p-shell knockout leading to ^{11}B) and continuum states (s-shell knockout, non-SRC correlations, etc.) with relative fractions of 53% and 36% respectively ($53\% + 36\% = 89\%$) [25]. Therefore, given that we measured 424 ^{12}C$(p, 2p)^{11}$B MF (p-shell knockout) events, we expect a total of $424 \cdot (11\%/53\%) = 88$ SRC events.

We estimate the experimental loss due to acceptance of the longitudinal momentum (see Extended Data Fig. 6a) as 50%, and another loss of 50% due to the strong cuts applied to select SRC events. Thus, in total, we expect to detect about $88 \cdot 50\% \cdot 50\% = 22$ SRC events.

If the SRC pair removal results in $A - 2$ fragments close to its ground-state, and assuming np-dominance (20 times more np than pp pairs) we expect a population of 90% ^{10}B and 10% ^{10}Be. We also considered that for a pp pair the knockout probability is twice larger than for pn. Using the estimation of 22 total SRC events will lead to 20 events for ^{10}B (we measure 26) and 2 events for ^{10}Be (we measure 3). These simple estimates show overall self-consistency in our data.

Last, as our selection cuts suppress, but do not eliminate events originating from the tail of the mean-field distribution, some events could result from de-excitation of high-$p_{\rm miss}$ ^{11}B fragments. To evaluate that fraction, we consider ^{11}B events that pass the SRC selection cuts (except for the exclusive missing mass cut). 39 such events are observed, of the total 424 MF ^{11}B events (i. e. a fraction of 9%). Reference [25] measured a neutron (proton) evaporation cross-section relative to the total continuum cross-section of 17% (7%). Using these fractions we expect a ^{10}B (^{10}Be) contribution from neutron (proton) evaporation based on the measured ^{11}B events of $39 \cdot (36\%/53\%) \cdot 17\% = 4$ events ($39 \cdot (36\%/53\%) \cdot 7\% = 2$). This is the maximum number that can be expected from this background, since for ^{10}B and ^{10}Be we apply an additional cut on the exclusive missing mass as explained above.

Extended Data

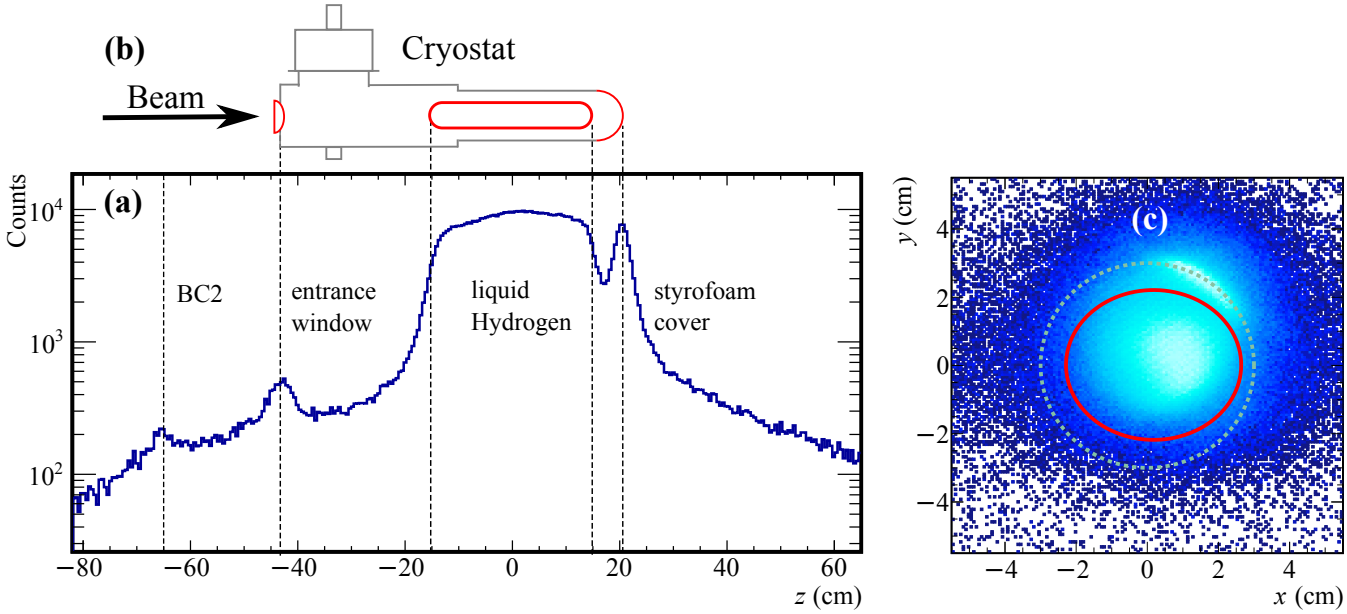

Extended Data Fig. 1. | Reaction Vertex. Reconstructed reaction vertex in the LH_2 target. The position along the beam line is shown in (a), scattering off in-beam material is also visible. For comparison, a sketch of the target device is shown in (b), scattering reactions are matched at the entrance window, the target vessel, styrofoam cover. A selection in $z < |13\text{ cm}|$ is applied to reject such reactions. The xy position at the reaction vertex is shown in (c), measured with the MWPCs in front of the target. The dashed line indicates the target cross section. Scattering at the target vessel at around ($x = 2\,\text{cm}$,$y = 2\,\text{cm}$) can be seen which is removed by the selection as indicated by the red circle.

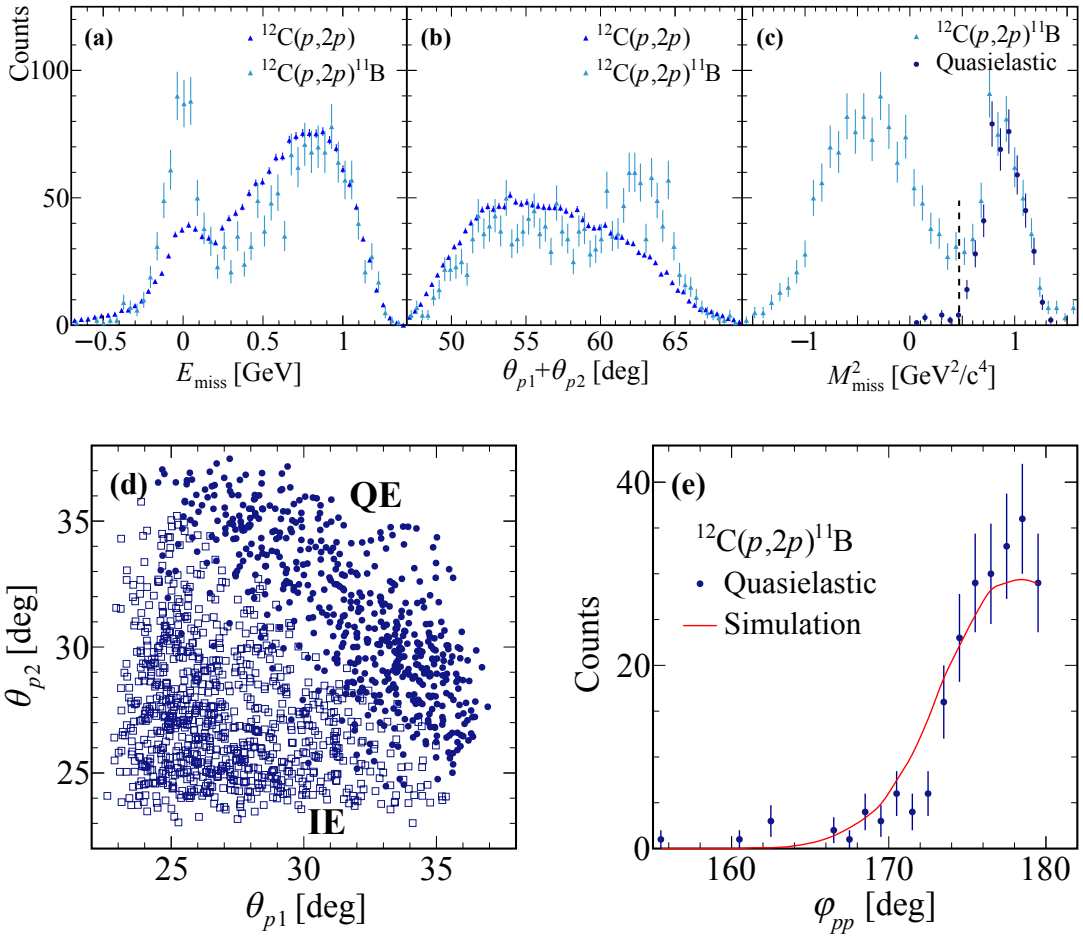

Extended Data Fig. 2. | **Single-Proton Knockout Signatures.** Projection in missing energy (a) and in-plane opening angle (b) of Fig. 2, comparing the inclusive reaction ^{12}C$(p, 2p)$ and tagged events with ^{11}B coincidence (the latter points are slightly offset for better visibility). The inclusive distribution is area normalized to the tagged one. The fragment selection clearly suppresses FSI, and the QE signal separates from IE. (c) Proton missing mass for tagged ^{12}C$(p, 2p)^{11}$B evens. After the QE selection in $E_{\rm miss}$ and in-plane opening angle, the distribution is shown in dark blue dots with artificial offset for better visibility. We apply an additional missing mass cut $M^2_{\rm miss} > 0.47$ GeV^2/c^4, indicated by the dashed line. (d) Angular correlation between the two $(p, 2p)$ protons for quasielastic ($M^2_{\rm miss} > 0.55$ GeV^2/c^4) and inelastic ($M^2_{\rm miss} < 0.55$ GeV^2/c^4) reactions only selected by missing mass. The QE events show a strong correlation with a polar opening angle of $\sim 63°$. (e) The off-plane opening angle for $M^2_{\rm miss} > 0.55$ GeV^2/c^4 peaks at 180° as expected. The width of this distribution is narrower than that dictated by the TAS acceptance.

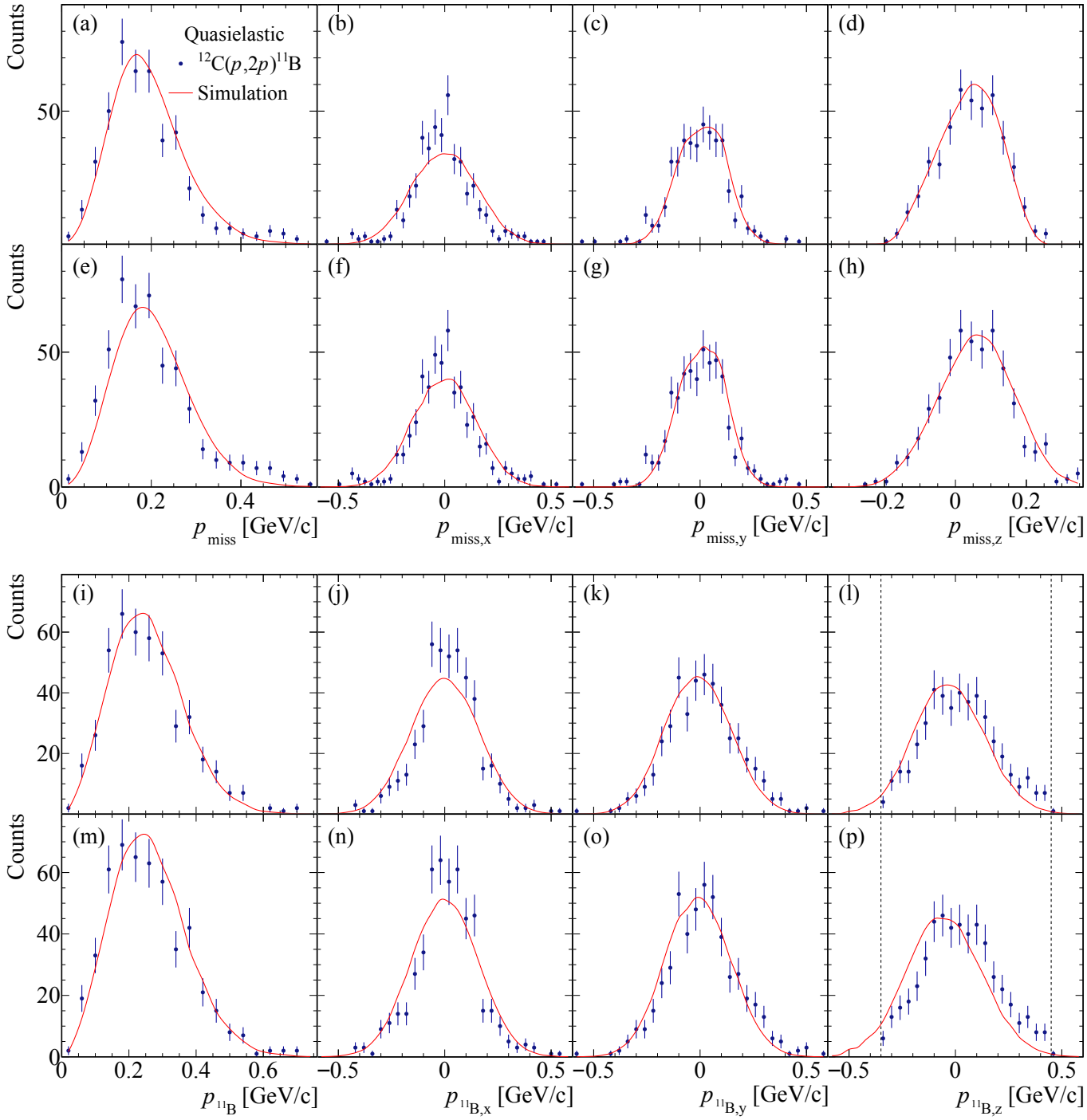

Extended Data Fig. 3. | **Missing and Fragment Momentum.** Momentum components for quasielastic ^{12}C$(p, 2p)^{11}$B reactions compared to simulation. The proton missing momentum is shown for (a)-(d), while (e)-(h) show the same distributions but with missing mass cut only (0.55 GeV^2/c^4 < $M^2_{\rm miss}$ <1.40 GeV^2/c^4). Agreement with the simulation is found in both cases. The shift in $p_{{\rm miss},z}$ is associated with a strong pp cross-section scaling with c.m. energy. For the same conditions the ^{11}B fragment momentum components are shown in (i)-(l), and (m)-(p). The dashed lines in $p_{^{11}{\rm B},z}$ indicate the momentum acceptance due to the fragment selection in P/Z.

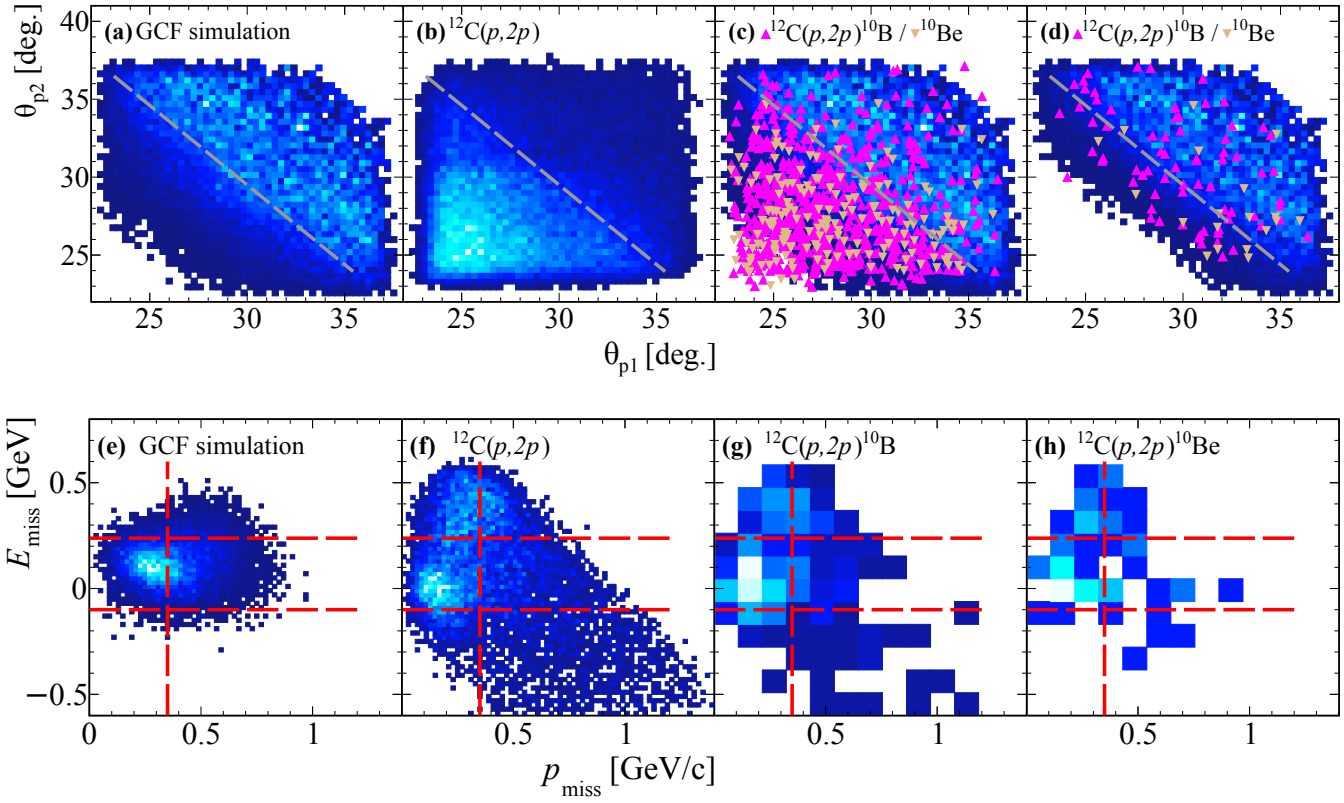

Extended Data Fig. 4. | **SRC Selection.** The proton-proton polar angular correlations are shown in (a)-(d) with $p_{\mathrm{miss}} > 350$ MeV/c, the in-plane opening angle cut to be applied is indicated by the dashed line: (a) GCF simulation, (b) ^{12}C$(p,2p)$ data, (c) ^{12}C$(p,2p)^{10}$B/Be data on top of simulation, and (d) the same as (c) but with additional E_{miss} cut. The missing energy vs. missing momentum is shown in (e)-(h): for (e) GCF simulation, (f) ^{12}C$(p,2p)$, (g) ^{12}C$(p,2p)^{10}$B, and (h) ^{12}C$(p,2p)^{10}$Be events that pass the in-plane opening angle cut. The selection cuts in -110 MeV$< E_{\mathrm{miss}} <$ 240 MeV and $p_{\mathrm{miss}} > 350$ MeV/c are indicated by the dashed lines.

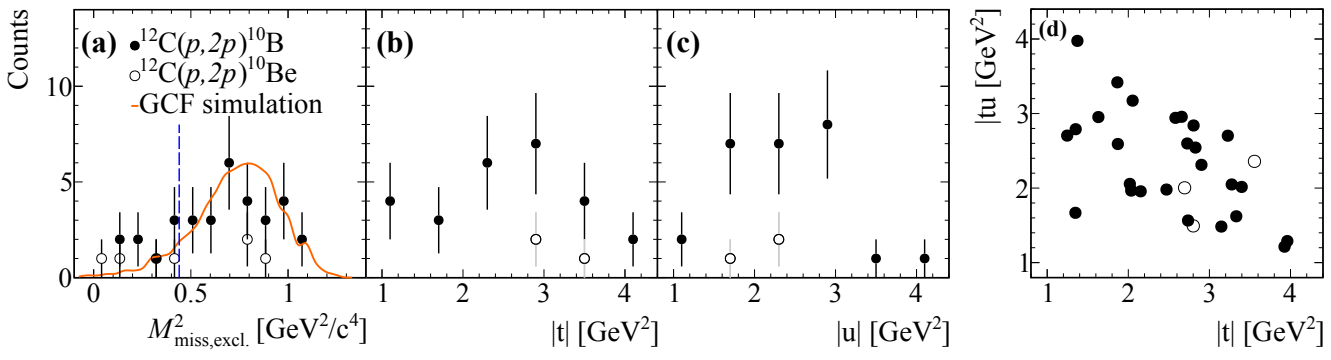

Extended Data Fig. 5. | **SRC Missing Mass and Momentum Transfer.** (a) The exclusive missing mass distributions for ^{12}C$(p,2p)^{10}$B events and ^{12}C$(p,2p)^{10}$Be events that pass the missing momentum, in-plane opening angle, and missing energy cuts together with the GCF simulation (orange). The blue line represents the applied cut on the exclusive missing-mass $M^2_{\mathrm{miss,excl.}} > 0.42$ GeV^2/c^4. (b) and (c) represent the Mandelstam variables for the same cases, ^{10}B and ^{10}Be, (d) shows the two-dimensional momentum-transfer plot for ^{10}B.

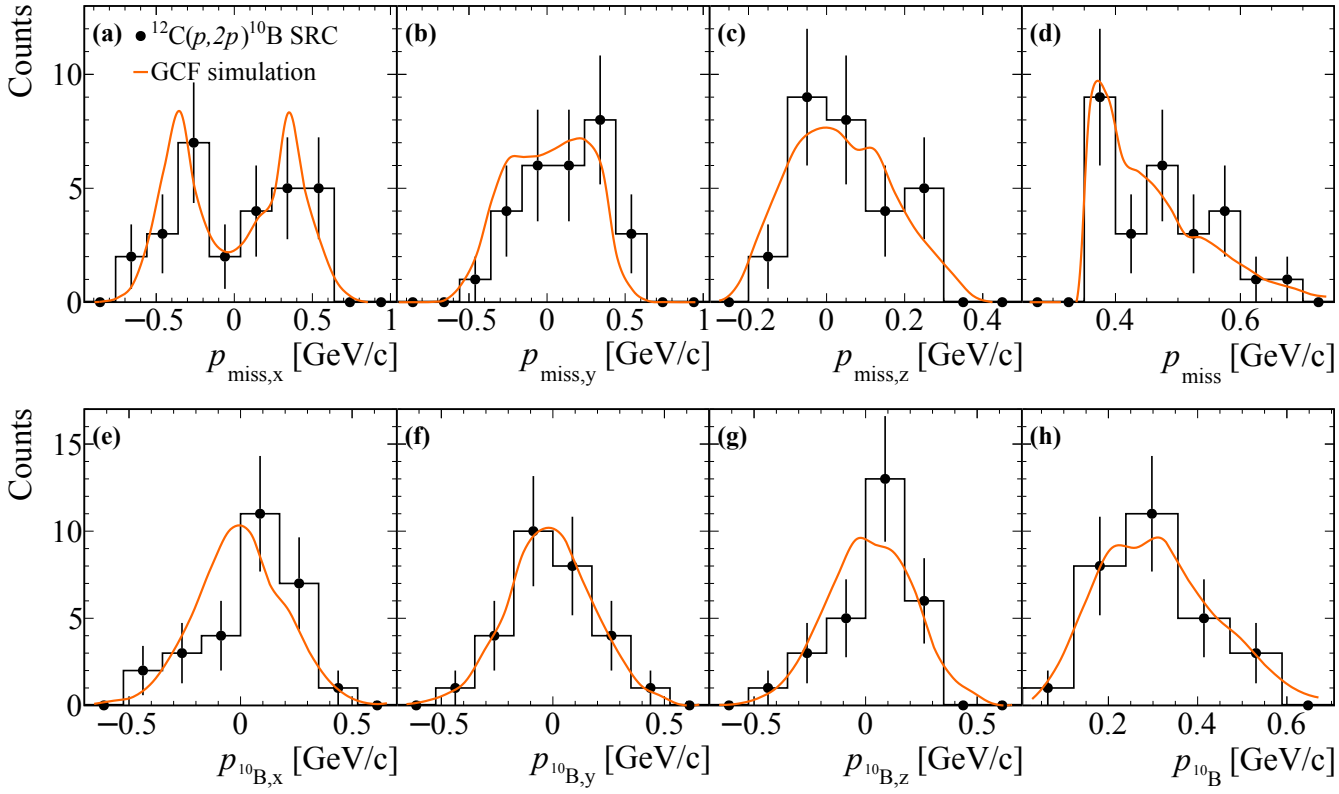

Extended Data Fig. 6. | **SRC Missing and Fragment Momentum.** The missing momentum distributions (a)–(d) for the selected ^{12}C$(p, 2p)^{10}$B SRC events (black) together with the GCF simulation (orange). Acceptance effects, especially in the transverse direction are well captured by the simulation. The lower figures (e)–(h) show the fragment momentum distributions in the rest frame of the nucleus for the same selected ^{12}C$(p, 2p)^{10}$B SRC events (black) together with the GCF simulation (orange).

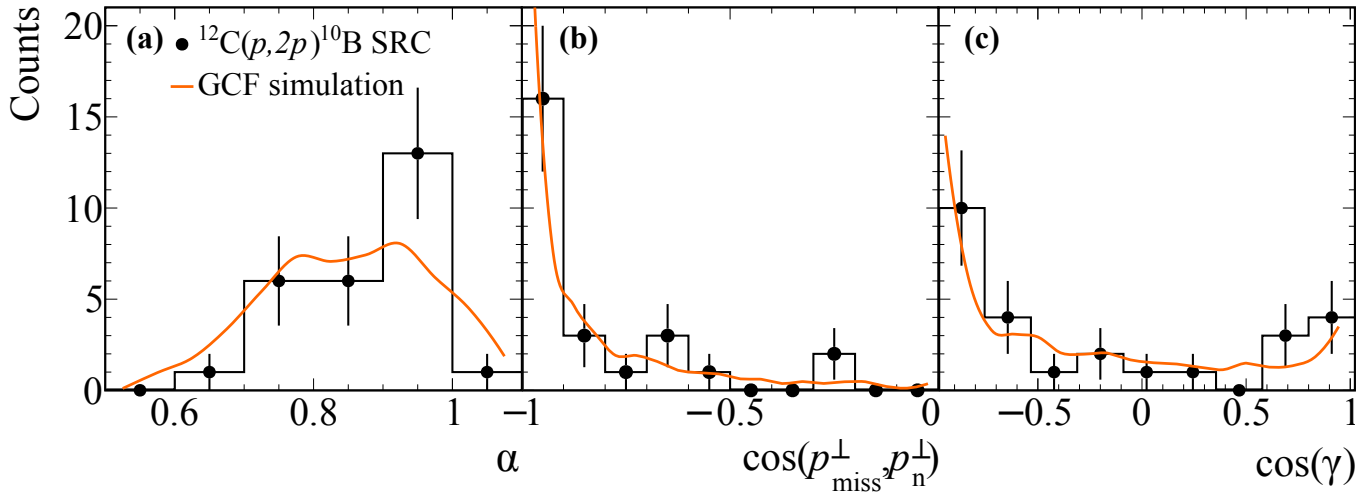

Extended Data Fig. 7. | **SRC Quantities.** Selected ^{12}C$(p, 2p)^{10}$B SRC events (black) together with the GCF simulation (orange). (a) Light-cone momentum distribution $\alpha = (E_{\rm miss} - p^z_{\rm miss})/m_p$. (b) Cosine of the opening angle between the missing momentum and the neutron reconstructed momentum in the transverse direction. (c) Cosine of the angle between the ^{10}B fragment and missing-momentum.

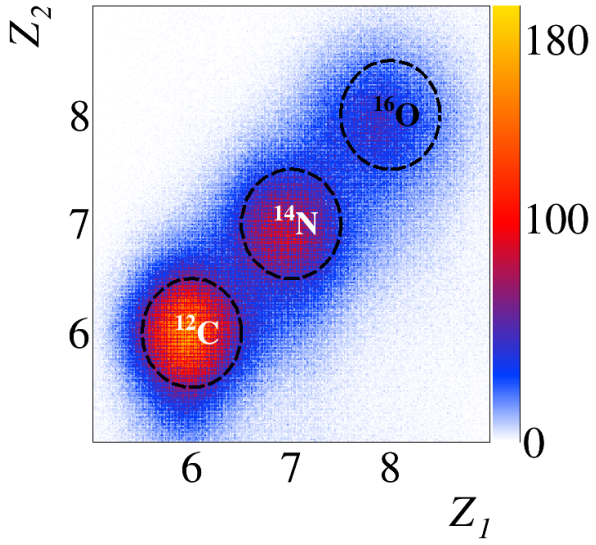

Extended Data Fig. 8. | **Incoming Beam Ions.** Charge identification of incoming beam ions measured event-wise using the two BC counters in front of the target (BC1, BC2). Besides ^{12}C, the $A/Z = 2$ nuclei ^{14}N and ^{16}O are mixed in the beam with less intensity.

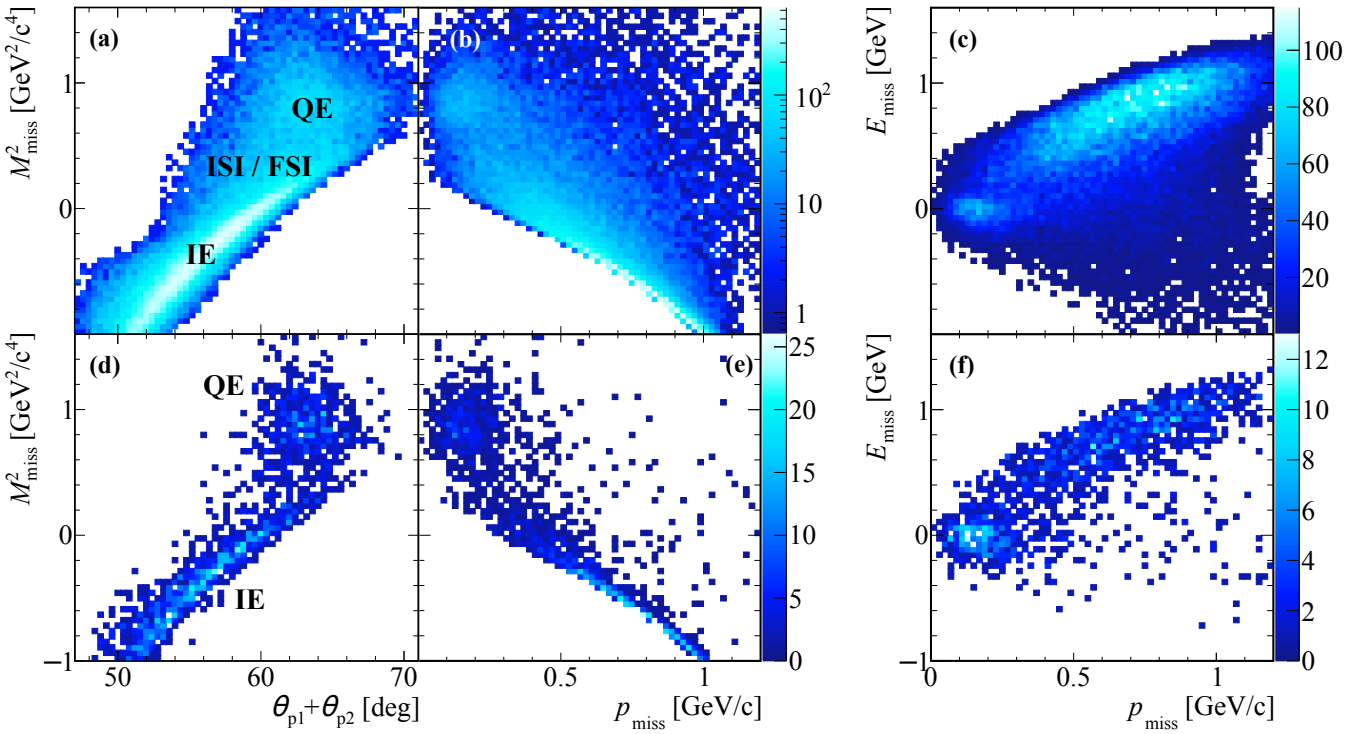

Extended Data Fig. 9. | **Kinematical Correlations in single-proton Knockout.** Figures (a)-(c) show the inclusive ^{12}C$(p, 2p)$ channel, and (d)-(f) the exclusive channel, i. e. with tagging ^{11}B. In both cases, the quasielastic peak (QE) and inelastic (IE) events are visible, while ISI/FSI are reduced by the fragment tagging. Eventually, a selection in E_{miss} and in-plane opening angle was chosen to select QE events, see Fig. 2. The distributions are not corrected for fragment-identification efficiency.

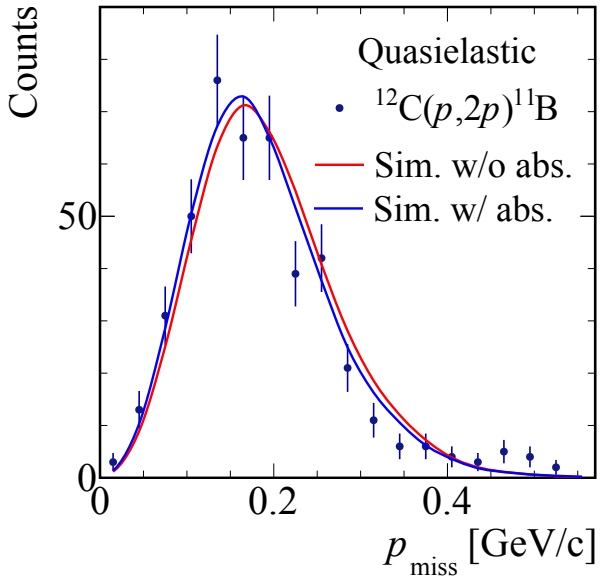

Extended Data Fig. 10. | **Mean Field Missing Momentum Calculations.** Missing-momentum distribution for quasielastic $^{12}\mathrm{C}(p,2p)^{11}\mathrm{B}$ events, as in Fig. 3 of the main text. The data are compared with single-proton knockout simulation based on momentum distributions from an eikonal calculation with and without including absorption effects in the calculation and normalized to the same integral as the data. Both curves agree with the measured data and show only a small difference.

Supplementary Materials for: Unperturbed inverse kinematics nucleon knockout measurements with a 48 GeV/c Carbon beam

1. BM@N Detector Configuration. The BM@N experimental setup at JINR allows to perform fixed-target experiments with high-energy nuclear beams that are provided by the Nuclotron accelerator [43]. Our experiment was designed such that in particular protons under large laboratory angles can be measured. That dictated a dedicated upstream target position and modified setup as used for studies of baryonic matter, but using the same detectors [44]. The setup comprises a variety of detection systems to measure positions, times, and energy losses to eventually obtain particle identification and determine their momenta. We are using scintillator detectors, multi-wire proportional chambers, Silicon strip detectors, drift chambers, gas-electron multipliers, and resistive plate chambers as shown in Fig. 1 and described in the following.

Beam Counters (BC): A set of scintillator counters, installed in the beam-line, based on a scintillator plate with an air light guide read in by a PMT were used. Two counters (BC1 and BC2) were located before the target: BC1 was located at the beam entrance to the experimental area. It is a 15 cm in diameter and 3 mm thick scintillator read out by a XP2020 Hamamatsu PMT. BC2 was located right in front of the target and provided the start time t_0. This scintillator is of 4 cm x 6 cm x 0.091 cm size, and was tilted by 45° so that its effective area was around 4 cm x 4 cm. It was read out by a Photonis MCP-PMT PP03656. Two counters (BC3 and BC4), each read out by a XP2020 PMT, were located downstream the target to measure the total charge of the fragment particles in each event. BC3 was based on 10 cm x 10 cm x 0.29 cm scintillator, and the BC4 was 7 cm x 7 cm x 0.3 cm. A veto-counter with the dimensions of 15 cm x 15 cm x 0.3 cm and a hole of 5 cm in diameter was located between BC2 and the target. It was read out by an XP2020 PMT and was included in the reaction trigger to suppress the beam halo.

Multi-wire proportional chambers (MWPC): We used two pairs of MWPC chambers, one before and one after the target for in-beam tracking [45]. Each chamber has six planes {X, U, V, X, U, V}. The X wires are aligned in y direction, U and V planes are oriented ±60° to X. The distance between wires within one plane is 2.5 mm, the distance between neighboring planes is 1 cm. In total 2304 wires are read out. The active area of each chamber is 500 cm^2 (22 cm x 22 cm). About 1 m separated the chambers in the first pair upstream the target and 1.5 m between the chambers in the second pair downstream the target. The polar angle acceptance of the chambers downstream the target is 1.46°. The efficiency of the MWPC pair in front of the target for particles with the charge of 6 is (92.2±0.1)%. The efficiency of the MWPC pair after the target is (88.8±0.7)% for ions with $Z = 6$, and (89.1±0.2)% for ions with $Z = 5$.

Silicon trackers (Si): As additional tracking system, three Silicon planes [46] were located after the target. In combination with the MWPCs after the target, an increased tracking efficiency is reached. The first and second Si planes share the same housing. The first plane consists of four modules, the second plane has two modules, the third plane has eight modules. Each module has 640 X-strips (vertical in y-direction) and 640 X'-strips (tilted 2.5° relative to X strips). The first plane has smaller modules with 614 X' strips and 640 X strips. The first two planes and the third plane are separated by 109 cm. The angular acceptance of the Si detector system is 1.58°. The design resolution of 1 mm for the y-coordinate and 50 μm for the x-coordinate was achieved in the experiment. The efficiency and acceptance of the Si tracking system, determined for reconstructed MWPC tracks before the target, is (81.5 ± 0.7)% for outgoing $Z = 6$ ions, and (82.6 ± 0.7)% for $Z = 5$ isotopes.

Combined tracks were reconstructed using information from the MWPC pair after the target and the Si detectors. The efficiency to find a Si track or a track in the second pair of the MWPC or a combined track, evaluated for events with reconstructed the track before the target, is (97.7 ± 0.2)% for $Z = 6$ ions, and (97.9 ± 0.3)% for $Z = 5$ isotopes.

Drift Chambers (DCH): Two large-area drift chambers, separated by 2 m, are located downstream the bending magnet. These detectors are used for tracking the charged fragments in the forward direction. Together with the upstream-tracking information of MWPC and Si in front of the magnet, the bending angle and thus the magnetic rigidity of the ions is determined. Each chamber consists of eight coordinate planes, twice {X, Y, U, V}, where X wires are perpendicular to the x-axis, Y wires are at 90° relative to X, and U and V are tilted by $+/-45°$, respectively. The distance between wires within one plane is 1 cm, in total 12,300 wires are read out. The spatial resolution, given as residual resolution, for one plane (X, Y, U, or V) is around 200 μm (1σ). It is obtained by the difference between the measured hit and the position from the reconstructed track at that plane. The efficiency of around 98% (97%) for each plane was estimated for the first (second) DCH based on the reconstructed matched track in the second (first) DCH. A reconstructed track within one DCH chamber has at least 6 points.

Two-Arm Spectrometer (TAS): In order to detect light charged particles from the target, scattered to large laboratory angles, the symmetric two-arm detection system around the beamline was constructed for this experiment. Each arm, placed horizontally at $+/-29.5°$ (center) with respect to the beamline, was configured by the following detectors along a 5 m flight length: scintillator – scintillator – GEM – RPC. Each arm holds one GEM (Gas-Electron

Multiplier) station at a distance of 2.3 m from the target. Each GEM station contained two GEM planes with the dimensions of 66 cm (x) x 40 cm (y) each, placed on top of each other (centered at $y = 0$) to increase the overall sensitive area to 66 cm x 80 cm. The spatial resolution of the GEM hit is 300 μm. Each RPC detector station, located at the end of the two arms at a distance of 5 m from the target, has a sensitive area of 1.1 m x 1.2 m. Each station consists of two gas boxes next to each other, each holds 5 multi-gap Resistive-Plate Chambers (RPCs) planes inside [47]. Two neighboring planes within one box overlap by 5 cm in y direction. Each plane has 30 cm long 1.2 cm wide horizontally aligned readout strips with a pitch of 1.25 cm. The measured x position is obtained by the time difference measured between the ends of one strip. The resolution is 0.6 cm. Together with the position information from the GEM, tracks are reconstructed along the arms and the time-of-flight information is taken from the RPC system. The clustering algorithm was applied to the neighboring strips fired in the same event. In addition, each arm was equipped with two trigger counters (TC), scintillator planes close to the target. The X planes consisted of two scintillators with dimensions of 30 cm x 15 cm x 0.5 cm located vertically side by side and read out by a Hamamatsu 7724 PMT each. The distance between the target center and the X-counters was 42 cm. Each Y plane was a single scintillator piece of 50 cm x 50 cm x 2 cm, read out by two ET9954KB PMTs. The distance between the target center and the Y planes was 170 cm. Each arm covers a solid angle of 0.06 sr, limited by the RPC acceptance.

Data Acquisition System (DAQ) and Triggers: The DAQ performs readout of the front-end electronics of the BM@N detectors event-by-event based on the information of the trigger system [48]. Timing information were read out from DCH and RPC (two-edge time stamp) and processed by Time to Digital Converters (TDC) based on HPTDC chip with typical accuracy of 20 ps for RPC and 60 ps for DCH. The amplitude information were read out from coordinate detector systems of Si and GEMs and processed by Amplitude to Digital Converters (ADC). The last 30 μs of waveforms were read back. The clock and time synchronization was performed using White Rabbit protocol. As mentioned in the main text, the reaction trigger was set up requesting an incoming and outgoing ion in coincidence with signals in the left and right arm trigger scintillator-counters (TC). Additional triggers are built from coincident signals in the various scintillator detectors, suited for either calibration purposes or data taking. The trigger matrix is shown in Table I, creating the so-called Beam trigger, and the physics triggers AndSRC and OrSRC. The input signals are BC1, BC2, and no veto signal (!V-BC). The coincidence condition AndXY requires signals in all TCs in the left and right arm, while OrXY takes the OR between the left and right arm of the spectrometer. The physics data were taken requesting the AndSRC trigger at a rate of about 180 Hz as measured during a beam pulse duration, allowing a livetime of close to 100%.

Supplementary Table I. | **Trigger Matrix.** Different coincidence triggers for collecting the data.

Trigger	BC1	BC2	!V-BC	AndXY	OrXY
Beam	x	x	x		
AndSRC	x	x	x	x	
OrSRC	x	x	x		x

2. Fragment Momentum Calculation Trajectories of charged particles are bent in the large analyzer magnet according to their magnetic rigidity, i. e. momentum-over-charge ratio $B\rho = P/Q$. This allows to determine the fragment total momenta.

For this purpose, simulations of the fragments, propagating in the magnetic field, were carried out using the standard field map of the magnet. The corresponding materials of the beam-line detectors were also implemented in the simulation. The simulated fragments were chosen to have the maximum possible position, angular and momentum spread to cover the entire geometrical acceptance of the magnet and detectors. The output of the simulation is used afterwards as a training sample for the multidimensional fit (MDF) algorithm [49] in the form of n-tuples which hold positions and angles of the fragment trajectory upstream and downstream of the magnet: $(x_0, y_0, z_0, \alpha_x, \alpha_y)$ and $(x_1, y_1, z_1, \beta_x, \beta_y)$ respectively. Performing MDF over the training sample yields an analytical fit function $P/Z^{mdf} = f(x_0, y_0, z_0, \alpha_x, \alpha_y, x_1, y_1, z_1, \beta_x, \beta_y)$, which can be applied to the positions and angles measured in the experiment.

In a similar way, a second MDF function for α_x angle was derived as $\alpha_x^{mdf} = g(x_0, y_0, z_0, \alpha_y, x_1, y_1, z_1, \beta_x, \beta_y)$. This function is used for the track-matching condition $(\alpha_x^{mdf} - \alpha_x)$=min, which allows to determine whether the tracks in upstream and downstream detection systems belong to the same global track through the magnet.

Having determined the two functions, α_x^{mdf} and P/Z^{mdf}, experimental data for the reference trajectory of unreacted ^{12}C is used to adjust the input variables' offsets, which reflect the alignment of the real detectors in the experimental setup with respect to the magnetic field. This is achieved by variation of the offsets in the experimental input variables simultaneously for α_x^{mdf} and P/Z^{mdf} until the residual between P/Z^{mdf} and its reference value is minimal. The reference value is chosen to be the P/Z of unreacted ^{12}C at the exit of the liquid-hydrogen target. Using

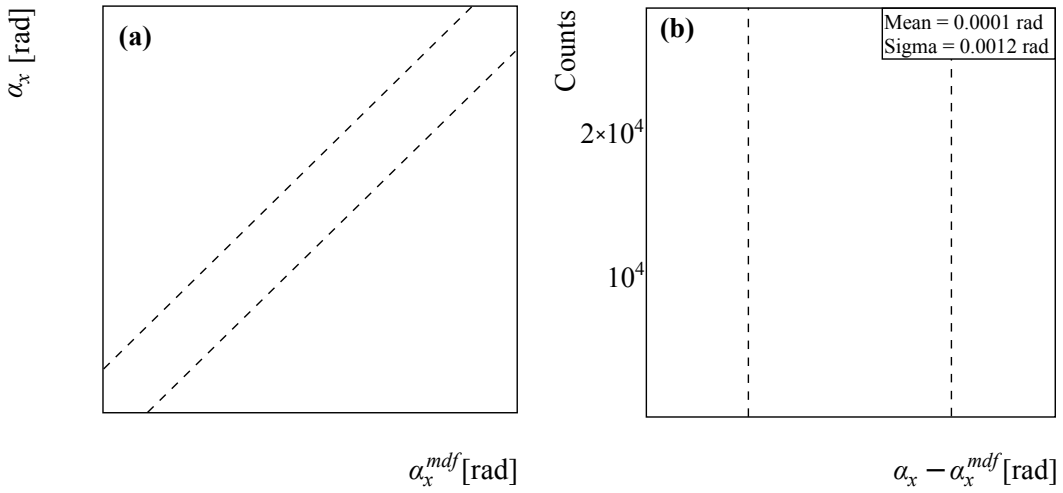

Supplementary Fig. 1. | **Track Matching.** (a) Correlation between α_x angle measured upstream of the magnet and the α_x^{mdf} reconstructed by the MDF. Dashed lines indicate applied cuts for the track matching condition. (b) Residual distribution $\alpha_x^{mdf} - \alpha_x$ and the applied cuts as in (a).

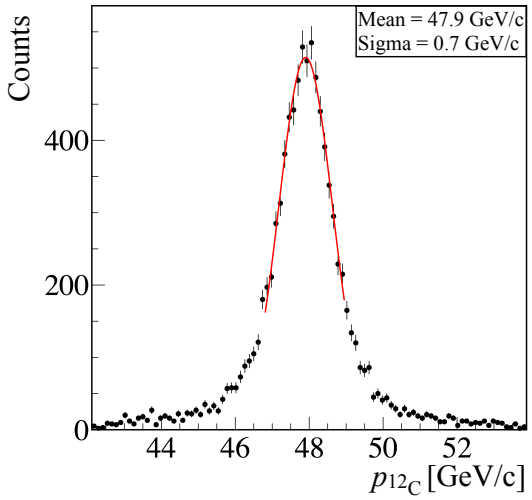

Supplementary Fig. 2. | **Fragment-Momentum Resolution.** Total momentum and its resolution for ^{12}C measured with empty target.

this approach a total-momentum resolution of 0.7 GeV/c for ^{12}C is achieved, as estimated with the empty target data, consistent with the resolution limits of the detection systems, see Fig. 2. The same momentum resolution was obtained for unreacted ^{12}C events, analyzed under the same conditions but with LH_2 target inserted. A width of $\sigma = 0.7$ GeV/c was measured with a reduced beam momentum of 47.6 GeV/c due to energy loss in the target and additionally straggling. The achieved momentum accuracy is evaluated to be 0.2%.

Fig. 1 shows the performance of the second MDF function for α_x. A global track is constructed when the reconstructed α_x^{mdf} falls within the 5σ gate indicated in the figure. In the analysis, only events with one global track, which combines the up- and downstream detectors, are considered (if not stated differently). In case of ^{11}B and ^{10}B only one charged-particle tracks are of interest. At this point we do not fully exploit the multi-track capability of this approach.

The fragment tracking efficiency is (50 ± 5)%, obtained for an empty target run and given with respect to the incoming and outgoing $Z = 6$ ion. This tracking efficiency includes the involved detector efficiencies, as well as the

reconstruction and matching efficiency of good tracks. We define the tracking efficiency for ^{12}C as ratio of events, incoming carbon $^{12}C_{in}$ vs. carbon downstream the target $^{12}C_{out}$, with

$$\epsilon_{\text{track}} = \frac{\#^{12}\text{C}_{\text{out}}}{\#^{12}\text{C}_{\text{in}}} = \frac{\#(\text{Good track})\&(Z_{\text{in}}=6)\&(Z_{\text{eff}}=6)}{\#(Z_{\text{in}}=6)\&(Z_{\text{eff}}=6)}, \quad (1)$$

where a "good track" is defined by

- Tracks in one of the upstream detector systems and in DCH.
- Exactly one reconstructed matched global track based on the combined information from upstream detectors and DCH as explained above.
- A "good" P/Z value: for $^{12}C_{out}$ the P/Z value is expected to be centered around 7.98 GeV/c (for beam momentum of 47.9 GeV/c), cf. Fig. 2. To determine the efficiency we examined different cuts in the range $(2-5)\sigma$ based on a Gaussian distribution in order to get an averaged value for the tracking efficiency. To identify the outgoing fragment in a similar way to the physics analysis we considered the 2D cut on P/Z vs. the energy deposit in BC4 and BC3, and checked for the systematics. The uncertainty is defined as the standard deviation resulting from those different cuts with respect to the mean value.

Table II lists the different contributions to the extracted efficiency. We adapt the same value for outgoing charge

Supplementary Table II. The different contributions for the tracking efficiency.

Good track	ϵ_{track}(%)
$Z_{\text{in}}=6$, $Z_{\text{eff}}=6$	100
Upstream track	98
DCH track	93
Upstream and DCH tracks	91
Global track	70
Good P/Z	50

$Z_{\text{eff}} = 4, 5$, in particular for ^{10}Be the only Be isotope of interest. The tracking efficiency is reduced by 24% due to the MDF algorithm with the applied matching criteria and the single global track condition. Another 28% inefficiency comes from our analysis selection cuts of a good P/Z. The reaction probability from in-beam material downstream the target was estimated to be smaller 5% and thus only contributes a small fraction to the latter condition. However, we estimated the uncertainty for B isotopes, and ^{10}Be using the experimental data. We looked at the fraction of ^{11,10}B (^{10}Be) from events with $Z_{\text{eff}} = 5$ ($Z_{\text{eff}} = 4$). $Z_{\text{eff}} = 5$ comes dominantly with ^{11}B or ^{10}B. We varied the fragment identification cuts to check the sensitivity of this fraction. This resulted in a very similar uncertainty to the ^{12}C, and therefore we adapt the same uncertainty.

$Z_{\text{eff}} = 4$ can come with several Be isotopes, or a combination of lighter fragments. In this case, to evaluate the uncertainty, we looked at the fraction of ^{10}Be from events with $Z_{\text{eff}} = 4$, and changed the identification cuts to evaluate the sensitivity. This resulted in $\sim 30\%$ difference (as opposed to 10% for C and B). Therefore, for ^{10}Be, we consider $\epsilon_{\text{track}} = (50 \pm 15)\%$.

For the overall fragment identification efficiency an additional $(83 \pm 6)\%$ efficiency for the measurement of the outgoing charge in BC3 and BC4 needs to be added.

3. Reaction-Vertex Reconstruction The reaction vertex is reconstructed whenever one track is reconstructed in each arm of the TAS. This requires at least one hit in the GEM and RPC systems to form a linear track in each arm. We consider only single-track options from the hit combinations. The coincident two tracks that come closest, formed from all possible hit combinations, determine the vertex position along the beamline in the z direction. Alignment procedures within the GEM-RPC system, the left and right arm, as well as relative to the incoming beam are applied. No particular reaction channel for absolute calibration purposes is available, therefore the detector positioning relies on a laser-based measurement, and the alignment relative to the other detector systems and the beam using experimental data. The quality of the tracks is selected according to their minimum distance, a selection criteria of better than 4 cm is applied in this analysis. Given the smaller angular coverage of the RPC system compared to the GEMs and detector inefficiencies, the track reconstruction efficiency is 40%, with an RPC detection efficiency of about 85%.

The position resolution in z was determined by placing three Pb foils separated by 15 cm at the target position. The reconstructed vertex position is shown in Fig. 3, clearly three distinct peaks at a distance of 15 cm representing the Pb foils are reproduced. Given the width of each peak, the z-position resolution from the two-arm spectrometer is on average 1.8 cm (1σ). Knowing the vertex and the position in the RPC, the flight length is determined.

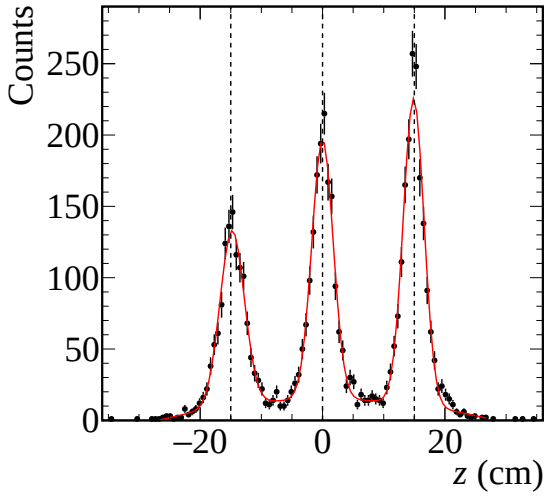

Supplementary Fig. 3. | **TAS Results.** Vertex in z direction for 3 Pb foils at the target position to determine the position resolution of the vertex reconstruction. The position resolution is 1.8 cm (1σ), the fit is shown by the red line (plus background). The dashed black lines indicate the absolute position alignment at $z = \pm 15$ cm and zero.

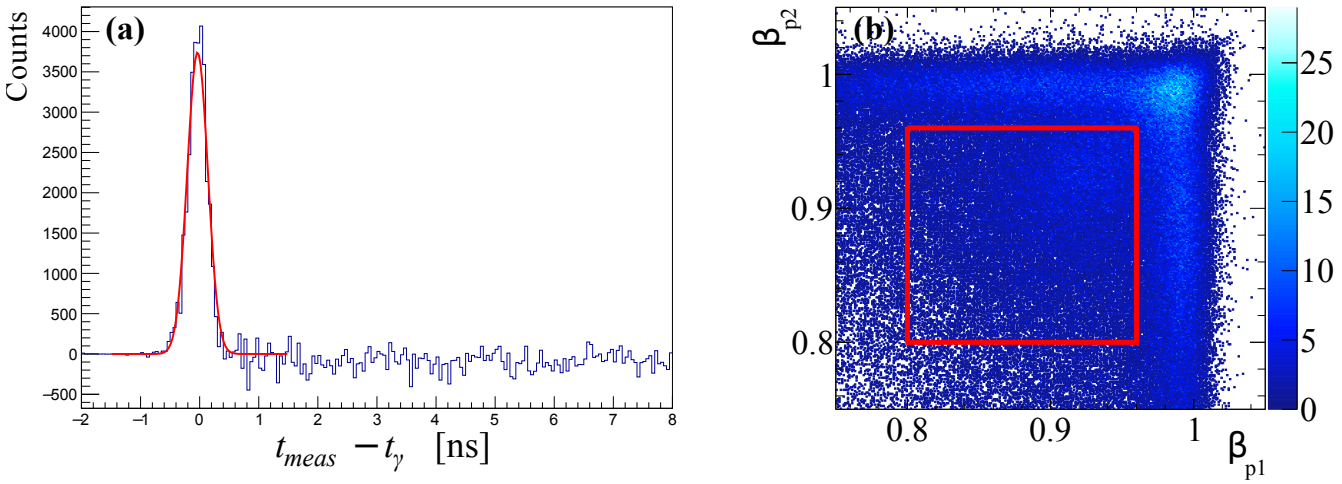

Supplementary Fig. 4. | **TAS Results.** (a) Result of RPC ToF calibration, γ peak arising in subtracted spectrum for Pb target runs with and without Pb sheets directly in front of RPC. The extracted ToF resolution is 175 ps ($1ß, \sigma$). (b) Basic velocity condition to select protons, the velocity cut in the left and right arm are indicated by the red lines.

4. ToF Calibration and proton momentum reconstruction resolution. The time-of-flight (ToF) calibration for the RPC is done by measuring gamma rays emitted from interactions with a single-foil Pb target. A 9 mm thick single Pb target was installed at the center position of the LH_2 target. In addition, a thin lead sheet was placed directly in front of the RPCs to convert gammas to charged particles. Measurements were done with and without the RPC lead sheet and the difference in the measured ToF spectrum for the two measurements was used to isolate gamma rays events. The subtracted ToF spectrum is shown in Fig. 4a, presenting a total ToF resolution (including the t_0 resolution) of 175 ps. Together with the time-of-flight that is measured between the start counter BC2 and the RPC, the total proton momentum can be determined. For a 2 GeV/c proton this corresponds to $\Delta\text{ToF}/\text{ToF} \sim 0.95\%$ which translates into a total-momentum resolution of 5.3% in the laboratory system and ~ 60 MeV/c for the missing momentum from the two protons in the ^{12}C rest frame.

Fig. 4b shows the β distribution of measured charged particles in the TAS with the initial velocity selection cut of $0.8 < \beta < 0.96$ applied for each particle shown as a red square.

[1] J. Kelly, Adv. Nucl. Phys. **23**, 75 (1996).
[2] L. Lapikas, Nuclear Physics A **553**, 297 (1993).
[3] D. Rohe *et al.* (E97-006 Collaboration), Phys. Rev. Lett. **93**, 182501 (2004).
[4] T. Kobayashi *et al.*, Nucl. Phys. A **805**, 431 (2008).
[5] T. Wakasa, K. Ogata, and T. Noro, Prog. Part. Nucl. Phys. **96**, 32 (2017).
[6] A. Gade *et al.*, Phys. Rev. C **77**, 044306 (2008).
[7] J. Tostevin and A. Gade, Phys. Rev. C **90**, 057602 (2014), arXiv:1409.6576 [nucl-th].
[8] L. Atar *et al.*, Phys. Rev. Lett. **120**, 052501 (2018).
[9] A. Schmidt *et al.* (CLAS), Nature **578**, 540 (2020), arXiv:2004.11221 [nucl-ex].
[10] G. Jacob and T. Maris, Rev. Mod. Phys. **38**, 121 (1966).
[11] P. Hansen and J. Tostevin, Ann. Rev. Nucl. Part. Sci. **53**, 219 (2003).
[12] W. Cosyn and J. Ryckebusch, Phys. Rev. C **80**, 011602 (2009), arXiv:0904.0914 [nucl-th].
[13] C. Ciofi degli Atti, Phys. Rept. **590**, 1 (2015).
[14] O. Hen, G. A. Miller, E. Piasetzky, and L. B. Weinstein, Rev. Mod. Phys. **89**, 045002 (2017).
[15] H. Feldmeier, W. Horiuchi, T. Neff, and Y. Suzuki, Phys. Rev. C **84**, 054003 (2011), arXiv:1107.4956 [nucl-th].
[16] R. Cruz-Torres, D. Lonardoni, R. Weiss, N. Barnea, D. W. Higinbotham, E. Piasetzky, A. Schmidt, L. B. Weinstein, R. B. Wiringa, and O. Hen, arXiv (2019), arXiv:1907.03658 [nucl-th].
[17] P. Spiller and G. Franchetti, Nucl. Instrum. Meth. A **561**, 305 (2006).
[18] "Frib400: The scientific case for the 400 mev/u energy upgrade of frib," `https://frib.msu.edu/_files/pdfs/frib400_final.pdf` (2019).
[19] B. Mukherjee, P. B. Patel, Z. Yan, R. J. Fletcher, J. Struck, and M. W. Zwierlein, Phys. Rev. Lett. **122**, 203402 (2019).
[20] I. Bloch, J. Dalibard, and W. Zwerger, Rev. Mod. Phys. **80**, 885 (2008).
[21] R. Cruz-Torres *et al.* (Jefferson Lab Hall A Tritium), Phys. Rev. Lett. **124**, 212501 (2020), arXiv:2001.07230 [nucl-ex].
[22] J.-W. Chen, W. Detmold, J. E. Lynn, and A. Schwenk, Phys. Rev. Lett. **119**, 262502 (2017), arXiv:1607.03065 [hep-ph].
[23] J. Lynn, D. Lonardoni, J. Carlson, J. Chen, W. Detmold, S. Gandolfi, and A. Schwenk, J. Phys. G **47**, 045109 (2020), arXiv:1903.12587 [nucl-th].
[24] A. Obertelli and T. Uesaka, Eur. Phys. J. A **47**, 105 (2011), arXiv:1109.5091 [nucl-ex].
[25] V. Panin *et al.*, Phys. Lett. B **753**, 204 (2016).
[26] E. Piasetzky, M. Sargsian, L. Frankfurt, M. Strikman, and J. W. Watson, Phys. Rev. Lett. **97**, 162504 (2006).
[27] R. Subedi *et al.*, Science **320**, 1476 (2008), arXiv:0908.1514 [nucl-ex].
[28] I. Korover, N. Muangma, O. Hen, *et al.*, Phys. Rev. Lett. **113**, 022501 (2014).
[29] O. Hen *et al.*, Science **346**, 614 (2014), arXiv:1412.0138 [nucl-ex].
[30] M. Duer *et al.* (CLAS Collaboration), Phys. Rev. Lett. **122**, 172502 (2019), arXiv:1810.05343 [nucl-ex].
[31] E. O. Cohen *et al.* (CLAS Collaboration), Phys. Rev. Lett. **121**, 092501 (2018), arXiv:1805.01981 [nucl-ex].
[32] I. Bobeldijk *et al.*, Phys. Rev. Lett. **73**, 2684 (1994).
[33] K. I. Blomqvist *et al.*, Phys. Lett. **B421**, 71 (1998).
[34] J. van Leeuwe, W. Hesselink, E. Jans, W. Kasdorp, J. Laget, C. Onderwater, A. Pellegrino, and J. Templon, Phys. Lett. B **523**, 6 (2001).
[35] F. Benmokhtar *et al.* (Jefferson Lab Hall A), Phys. Rev. Lett. **94**, 082305 (2005), arXiv:nucl-ex/0408015.
[36] L. Frankfurt, M. Sargsian, and M. Strikman, Int. J. Mod. Phys. A **23**, 2991 (2008), arXiv:0806.4412 [nucl-th].
[37] V. Kekelidze, A. Kovalenko, R. Lednicky, V. Matveev, I. Meshkov, A. Sorin, and G. Trubnikov, Nucl. Phys. A **904-905**, 945c (2013).
[38] N. N. A. et al., in *Cryogenics 2019. Proceedings of the 15th IIR International Conference: Prague, Czech Republic, April 8-11, 2019.* (2019).
[39] T. Aumann, C. Bertulani, and J. Ryckebusch, Phys. Rev. C **88**, 064610 (2013), arXiv:1311.6734 [nucl-th].
[40] M. Hussein, R. Rego, and C. Bertulani, Phys. Rept. **201**, 279 (1991).
[41] A. Ozawa, T. Suzuki, and I. Tanihata, Nucl. Phys. A **693**, 32 (2001).
[42] G. Alkhazov, S. Belostotsky, and A. Vorobev, Phys. Rept. **42**, 89 (1978).
[43] M. Kapishin (BM@N), Nucl. Phys. A **982**, 967 (2019).
[44] "Conceptual design report bm@n — baryonic matter at nuclotron," ().
[45] S. Khabarov, E. Kulish, V. Lenivenko, A. Makankin, A. Maksymchuk, V. Palichik, M. Patsyuk, S. Vasiliev, A. Vishnevskij, and N. Voytishin, EPJ Web Conf. **201**, 04002 (2019).
[46] Y. Kovalev, M. Kapishin, S. Khabarov, A. Shafronovskaia, O. Tarasov, A. Makankin, N. Zamiatin, and E. Zubarev, Journal of Instrumentation **12**, C07031 (2017).
[47] V. Babkin *et al.*, Nucl. Instrum. Meth. A **824**, 490 (2016).
[48] "Bm@n daq system," ().
[49] "Root cern: Multi-dimensional fit," `https://root.cern.ch/doc/master/classTMultiDimFit.html`.